Journal of
Mechanics of
Materials and Structures

TWO COMPLEMENTARY TRIOS MATERIAL MODEL AND EXPERIMENTAL SIMULATIONS OF SAE 4340 AND RHA

Chein-Shan Liu, Hong-Ki Hong and Ya-Po Shiao

Volume 2, Nº 5 May 2007

mathematical sciences publishers

JOURNAL OF MECHANICS OF MATERIALS AND STRUCTURES
Vol. 2, No. 5, 2007

TWO COMPLEMENTARY TRIOS MATERIAL MODEL AND EXPERIMENTAL SIMULATIONS OF SAE 4340 AND RHA

CHEIN-SHAN LIU, HONG-KI HONG AND YA-PO SHIAO

A two-complementary-trio material model for cyclic plasticity is proposed in this paper. In this formulation we consider a contact surface to confine the motion of contact stress. While the on-off switching criteria of plasticity are derived from the first complementary trio, the switching criteria of kinematic hardening rules are derived according to the second complementary trio. In terms of the new concept of contact stress and contact surface, it becomes easier to derive the governing rule of back stress during the contact of yield surface and bounding surface. The validity of the new model is confirmed by comparing the computational results with the experimental data for materials of SAE 4340 and RHA under uniaxial cyclic tests and biaxial cyclic tests. Even though the material constants used in the new model are parsimonious (with only 12), it is immediately recognized that the cyclic response curves described by the new model are in good agreement with the experimental data.

1. Introduction

Simulations using the conventional J_2 mixed-hardening plasticity model reveal an over-square phenomenon in the bending corners of the stress-strain curve [Liu 2004], which definitely does not match the most experimental results. This shortcoming may be attributed to the fact that in conventional plasticity the plastic modulus has the same value at all the stress points on the yield surface. In order to address this limitation, many researchers have introduced different nonlinear kinematic hardening laws [Liu 2005], in the context of single surface plasticity theory.

An elastic/plastic model with a unique yield surface has severe limitations as pointed out by Liu [2006]: (a) a discontinuous stress rate and strain rate relation is predicted, which changes abruptly when stress reaches the yield surface, (b) upon loading, the consistent condition requires the subsequent stress points to remain on the yield surface, and (c) the hysteresis loop for a partial unloading-reloading cycle, the Masing effect and the strain ratcheting phenomenon cannot be described properly.

To remedy these limitations, various unconventional constitutive models have been proposed for simulating the cyclic behavior of materials in the past few decades. In contrast to the conventional single yield-surface plasticity theory, Mróz [1967] has proposed a multisurface model with an associated kinematic hardening rule. Thereafter, while a simplified two-surface model employing a yield surface and only one subyield surface enclosing a purely elastic domain was formulated by Dafalias and Popov [1975; 1976], Krieg [1975], Mróz et al. [1979], Tseng and Lee [1983], and Hashiguchi [1988], the infinite-surface model was developed by Mróz et al. [1981], and the subloading surface model was developed by Hashiguchi [1989].

Keywords: cyclic plasticity, two complementary trios.

Two-surface theories originate from a nesting-surface model proposed by Mróz [1967]. In practical applications, there have been several versions of two-surface theories, which are in general supported by different experimental investigations. Basically, these theories aim to make the plastic modulus a more flexible mechanism to fit the experimental results, so that it can be used to predict the material behavior more appropriately.

For example, Dafalias and Popov [1975; 1976] have introduced the concept of *bounding surface* to assert that there exist three regions at which the plastic modulus first takes the value infinity as the stress point first attaches to the yield surface; then, when it pushes and moves together with the yield surface the plastic modulus decreases smoothly; and finally, the plastic modulus becomes a constant in the third region. The last region is called the bounding surface. At the same time, Krieg [1975] has proposed a two-surface theory more similar to the multisurface theory of Mróz, which assumed many nonintersecting yield surfaces. In addition to a yield surface, Krieg [1975] introduced a limiting surface to delineate the plastic modulus of material at the reversal loading direction. This theory can be viewed as a continuous version of the discrete multisurface model of Mróz.

Ohno and Wang [1991] have shown that the nonlinear kinematic hardening rule with back stress decomposed into multicomponents can be transformed into a multisurface form, and that the transformed multisurfaces are nested and obey the Mróz-type translation rule without intersecting each other.

The existence of a bounding surface has been supported by experimental work [Phillips and Sierakowski 1965; Phillips and Tang 1972; Phillips and Kasper 1973; Phillips and Moon 1977]. The plastic behavior of material is governed by two surfaces: the yield surface and the bounding surface. According to the investigations made by these authors, two important phenomena can be observed.

The first is that the behavior on the bounding surface tends to satisfy the isotropic hardening rule and the normality principle, which indicates that when the stress approaches the bounding surface, the plastic strain rate will align its direction to the normal direction of the bounding surface.

The second is that the yield surface cannot penetrate the bounding surface, and they can be in contact at most. When the yield surface is in contact with the bounding surface, the motion of yield surface must be modified to avoid the penetration of the bounding surface, and thus the motion of yield surface does not necessarily abide by Prager's kinematic hardening rule [Prager 1956].

The possibilities of intersection of yield and bounding surfaces have been examined by McDowell [1989] in the framework of two-surface plasticity theory. Intersections are undesirable from the perspectives of both computational implementation and agreement with experimental results. McDowell [1989] has shown that the intersections may occur even for the commonly employed formulations for certain loading histories. Therefore, in the development of a two-surface plasticity model it is important to avoid intersection. Recently, the multisurface plasticity models were developed and applied by Elgamal et al. [2003], Khoei and Jamali [2005], and Abdel-Karim [2005].

A correct simulation of cyclic phenomena is still one of the most difficult problems, and there are many complex constitutive models that allow one to simulate the cyclic behavior appropriately. See, for example, [Chaboche 1991; 1994; Voyiadjis and Sivakumar 1991; 1994; Hassan and Kyriakides 1992a; 1992b; Ohno and Wang 1993a; 1993b; 1994; Abdel-Karim and Ohno 2000; Ohno and Abdel-Karim 2000; Bari and Hassan 2001; 2002; Voyiadjis and Abu Al-Rub 2003; Chen and Jiao 2004; Vincent et al. 2004; Dieng et al. 2005; Chen et al. 2005; Liu 2006]. This list reflects just some of the active research dealing with the cyclic behaviors of materials, and improvements are still in progress.

Evolutions of yield surface and plastic strain increments have been investigated by Wu [2003] from the perspective of Prager's linear kinematic hardening rule, and it was found that the plastic strain increment vector is normal to the yield surface and its magnitude and direction vary as the stress path is traversed. Liu and Chang [2005] have studied the material models endowed with the anisotropic quadratic yield criteria from a noncanonical Minkowski frame to enhance the computational accuracy. However, many higher-order nonquadratic yield criteria have been proposed to simulate the distortion of yield surfaces during plastic deformation, which is an important issue in plasticity theory; see, for example, [François 2001; Chiang et al. 2002; Bron and Besson 2004; Cazacu and Barlat 2004; Kowalczyk and Gambin 2004; Vincent et al. 2004; Liu and Chang 2004; Wu et al. 2005; Yeh and Lin 2006; Christensen 2006].

For the simulation of cyclic loading phenomena and strain induced anisotropy, the present method introduces a two-complementary-trio mechanism. Usually, only one complementary-trio is employed in the conventional plasticity theory [Liu 2004]. In the following we first give the basic hypotheses underlying the new model in Section 2. A distance function is derived to control the plastic modulus. In Section 3, some demonstrations are given to rewrite the model in terms of the back stress and the eccentric stress (the center of the bounding surface). In Section 4, we discuss the weak stability criteria of the new model, where a rather detailed description about the material functions is given. According to the first complementary trio, we derive the switching criteria of plasticity in Section 5. Then, according to the second complementary trio we derive the switching criteria of kinematic hardening rules in Section 6. In Section 7, we give a procedure to determine the coefficient functions appearing in the kinematic hardening rule. In Section 8, we discuss the plastic modulus. In Sections 9 and 10, we show and discuss the experimental results of SAE 4340 and RHA. In Section 11, the comparisons between theoretical and experimental results are given. In Section 12, we prove the convexity of the distance function and derive a yield surface with a prescribed strain offset. It is shown that the two-complementary-trio model can properly account for deformation induced anisotropy, where by using an offset of strain [Wu 2005] to delineate the yield point, we can produce nonquadratic yield loci in the stress plane. Finally, some conclusions are given in Section 13.

2. The postulations

The internal variables theory has played a key role in the development of plastic constitutive equations. The internal variables widely employed are: the back stress locating the center of the yield surface in the stress space; the parameters that characterize the expansion/contraction of the yield surface; the parameters that characterize the bounding surface in multisurface plasticity theories, etc. However, these specifications of the constitutive relations may be not self-consistent, unless the specific model is so designed. In particular, we have mentioned the possible intersection of the yield surface and the bounding surface in two-surface theories. Therefore, how to develop a two-surface theory that can avoid the intersection automatically may be a significant work. Although, Ohno and Wang [1991] have solved this problem for a multisurface theory with a different approach, it is worthwhile to propose a two-surface plasticity model that does not have the intersection problem.

It is known that the complementary trio in a single-yield surface theory plays a vital role in confining the stress point to a location within the yield surface. This concept can be employed and extended to cover the two-surface theory. In addition to the first complementary trio, we can introduce the second

complementary trio to govern the motion of a newly defined "contact stress", which is the difference of the back stress (the center of the yield surface) with respect to the eccentric stress (the center of the bounding surface). Therefore, with a different approach than before, we can propose a new plastic flow rule and evolution laws of active stress and contact stress such that the intersection of yield and bounding surfaces can be avoided automatically.

We construct such a two-complementary-trio cyclic elastoplasticity model by using the following hypotheses:

$$\dot{e}_{ij} = \dot{e}^e_{ij} + \dot{e}^p_{ij}, \tag{1}$$

$$s_{ij} = s^d_{ij} + s^c_{ij} + s^a_{ij}, \tag{2}$$

$$\dot{s}_{ij} = 2G\dot{e}^e_{ij}, \tag{3}$$

$$\dot{e}^p_{ij} = \frac{3\dot{\lambda}_a}{2h_a}s^a_{ij} + \frac{3\dot{\lambda}_c}{2h_c}s^c_{ij}, \tag{4}$$

$$\dot{s}^a_{ij} = -C_1\dot{\lambda}_c s^a_{ij} - \left(\frac{2}{3}k'_a + \gamma_c C_2\right)\dot{e}^p_{ij} - C_3\dot{\lambda}_c e^p_{ij} + (1-\gamma_c)\dot{s}_{ij} + C_4\dot{\lambda}_c s_{ij}, \tag{5}$$

$$\dot{s}^c_{ij} = -C_1\dot{\lambda}_c s^c_{ij} + \left(\frac{2}{3}k'_c + \gamma_c C_2\right)\dot{e}^p_{ij} + \gamma_c\dot{s}_{ij}, \tag{6}$$

$$f_a \le 0, \tag{7}$$

$$\dot{\lambda}_a \ge 0, \tag{8}$$

$$\dot{\lambda}_a f_a = 0, \tag{9}$$

$$f_c \le 0, \tag{10}$$

$$\dot{\lambda}_c \ge 0, \tag{11}$$

$$\dot{\lambda}_c f_c = 0, \tag{12}$$

in which e_{ij}, e^e_{ij}, e^p_{ij}, s^a_{ij}, s^c_{ij}, s^d_{ij} and s_{ij} are respectively the deviatoric tensors of strain, elastic strain, plastic strain, active stress, contact stress, eccentric stress and stress. Here,

$$f_a := \sqrt{\frac{3}{2}s^a_{ij}s^a_{ij}} - h_a \tag{13}$$

is the von Mises yield function, and

$$f_c := \sqrt{\frac{3}{2}s^c_{ij}s^c_{ij}} - h_c \tag{14}$$

is a corresponding contact function of the same form with f_a.

In Equations (1), (3)–(6), (8), (9), (11) and (12) the rates are obtained by taking the derivatives with respect to time. However, all the dt can be factored out to obtain an incremental form of these equations because the model is rate-independent; if we employ another time scale, say t', with $dt'/dt > 0$, in these equations, it does not change the response.

It deserves to be noted that the plastic flow rule in Equation (4) is different from the conventional one by virtue of an extra term which is proportional to the contact stress. However, this term is active only when the yield surface is in contact with the bounding surface. Before such contact, equation (4) follows the associated flow rule.

The material functions are dependent on the equivalent plastic strain $\bar{e}^p$ defined by

$$\bar{e}^p = \int_{t_0}^{t} \dot{\bar{e}}^p(\xi)d\xi,\ \ \dot{\bar{e}}^p := \left(\frac{2}{3}\dot{e}^p_{ij}\dot{e}^p_{ij}\right)^{\frac{1}{2}} \geq 0. \tag{15}$$

It can be seen that $\bar{e}^p$ is a time-like parameter because its time derivative $\dot{\bar{e}}^p$ is nonnegative, and hence is an indicator of the irreversible change of material properties.

In the above equations, $\dot{\lambda}_c$ is defined as

$$\dot{\lambda}_c := \gamma_c \dot{\bar{e}}^p, \tag{16}$$

with

$$\gamma_c := \frac{s^c_{ij}}{\sqrt{\frac{2}{3}}h_c}\frac{s^a_{ij}}{\sqrt{\frac{2}{3}}h_a} - \frac{h'_c}{k'_c}. \tag{17}$$

The above definition of γ_c will be derived in Section 6.

The material functions h'_a, k'_a, h'_c and k'_c are assumed to be related by

$$(h'_a + k'_a)\left(1 - \exp\left(a\left(\frac{\mathscr{D}}{2h_c}\right)^b\right)\right) = (h'_c - k'_c)\exp\left(a\left(\frac{\mathscr{D}}{2h_c}\right)^b\right), \tag{18}$$

where $a \geq 0$ and $b \geq 0$ are two material constants, and

$$\mathscr{D} = -\frac{(s^a_{ij} + s^c_{ij})\dot{e}_{ij}}{\sqrt{\frac{2}{3}\dot{e}_{mn}\dot{e}_{mn}}} + \sqrt{\frac{((s^a_{ij} + s^c_{ij})\dot{e}_{ij})^2}{\frac{2}{3}\dot{e}_{mn}\dot{e}_{mn}} + (h_a + h_c)^2 - \frac{3}{2}(s^a_{ij} + s^c_{ij})(s^a_{ij} + s^c_{ij})} \tag{19}$$

is a distance function between the stress point s_{ij} and its image point on the bounding surface along the strain rate direction $\dot{e}_{ij}$, as shown in Figure 1. The bounding surface is a surface in the stress space with center s^d_{ij} and radius $h_a + h_c$, whereas the contact surface is a surface with center s^d_{ij} and radius h_c. When $f_a = 0$ and $f_c = 0$, the yield surface is in contact with the bounding surface. Figure 1 shows a noncontact case.

The projection of $s^a_{ij} + s^c_{ij}$ onto the unit tensor along the direction $\dot{e}_{ij}$ is denoted by

$$d_1 = \frac{(s^a_{ij} + s^c_{ij})\dot{e}_{ij}}{\sqrt{\frac{2}{3}\dot{e}_{mn}\dot{e}_{mn}}}. \tag{20}$$

From Figure 1 we can obtain the following relation:

$$(\mathscr{D} + d_1)^2 + d_2^2 = (h_a + h_c)^2, \tag{21}$$

where

$$d_2^2 = \frac{3}{2}(s^a_{ij} + s^c_{ij})(s^a_{ij} + s^c_{ij}) - d_1^2. \tag{22}$$

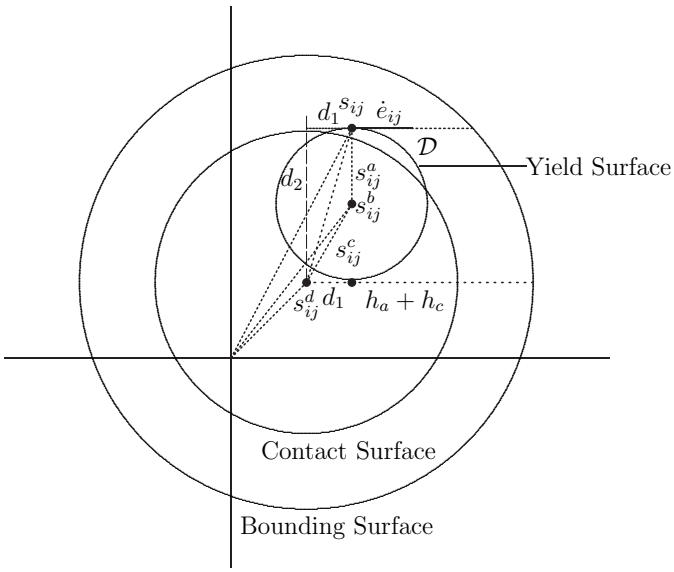

Figure 1. The distance between the current stress point and the image point on the bounding surface along a strain rate direction.

Therefore, from (20)–(22) we can derive Equation (19).

We also suppose that

$$G > 0,\ h_a > 0,\ h_c > 0,\ h'_c > 0,\ k'_c > 0. \tag{23}$$

A detailed description of these material functions is given in Section 4.

3. Comments on postulations

The evolution rules proposed for s^a_{ij} and s^c_{ij} in (5) and (6) may be replaced by the following differential equations for s^b_{ij} and s^d_{ij}:

$$\dot{s}^b_{ij} = -C_1\dot{\lambda}_c s^b_{ij} + \left(\frac{2}{3}k'_a + \gamma_c C_2\right)\dot{e}^p_{ij} + C_3\dot{\lambda}_c e^p_{ij} + \gamma_c \dot{s}_{ij} + (C_1 - C_4)\dot{\lambda}_c s_{ij}, \tag{24}$$

$$\dot{s}^d_{ij} = -C_1\dot{\lambda}_c s^d_{ij} + \frac{2}{3}(k'_a - k'_c)\dot{e}^p_{ij} + C_3\dot{\lambda}_c e^p_{ij} + (C_1 - C_4)\dot{\lambda}_c s_{ij}, \tag{25}$$

in which

$$s^b_{ij} := s^c_{ij} + s^d_{ij}$$

is called the back stress.

The above representation in terms of back stress and the center of bounding surface is schematically shown in Figure 1. It is interesting to note that both s^d_{ij} and s^b_{ij} play the role of a back stress; while s^d_{ij} is a back stress of contact surface (or bounding surface), s^b_{ij} is known to be a back stress of the yield surface. It is also interesting to note that both s^c_{ij} and s^a_{ij} play the role of a relative stress; while s^c_{ij} is a relative stress between s^b_{ij} and s^d_{ij}, s^a_{ij} is known to be a relative stress between stress s_{ij} and back stress s^b_{ij}. More frequently, s^a_{ij} is called the active stress. In the two complementary trios model, there are two

surfaces, the yield surface and the contact surface (or bounding surface); two back stresses, s^b_{ij} and s^d_{ij}; and two relative stresses, s^a_{ij} and s^c_{ij}.

It is observed that (9) and (12) constitute the Kuhn–Tucker conditions [Rockafellar 1970] for the following constrained optimization problem: minimize $-\sigma_{ij}\dot{\epsilon}^p_{ij}$ subject to (7) and (10). In other words, the plastic-flow rule (4), the equalities $\dot{\lambda}_a f_a = 0$ and $\dot{\lambda}_c f_c = 0$, and the inequalities $\dot{\lambda}_a \geq 0,\ f_a \leq 0$ and $\dot{\lambda}_c \geq 0,\ f_c \leq 0$ are sufficient and necessary for the assertion of maximum plastic power for the set of admissible stress states. Because these conditions are the hypotheses of the new model, we have proved the assertion for the conditional *associativity/nonassociativity* of the new model. The *associativity* refers to that $\partial f/\partial\sigma_{ij} = c\partial g/\partial\sigma_{ij}$, where c is a positive real and g is a certain plastic potential function. Conversely, the *nonassociativity* refers to that $\partial f/\partial\sigma_{ij} \neq c\partial g/\partial\sigma_{ij}$ for any positive real c. In the present model the plastic flow is associated under the condition of ($f_c < 0$) or ($f_c = 0$ and $\gamma_c = 0$). Otherwise, it is nonassociated.

For the two complementary trios represented by (7)–(12), there exist two *switching criteria* that characterize the values of $\dot{\lambda}_a$ and $\dot{\lambda}_c$. The details of deriving some suitable switching criteria to control them will be given in Section 5. However, for use in the next section, we will call the one that controls $\dot{\lambda}_a$ the first switch, and that which controls $\dot{\lambda}_c$, the second switch.

As seen from (24) the present model may have a rather complex kinematic hardening rule. However, as will be discussed in Section 7, we can greatly simplify this kinematic hardening rule in view of the concept of contact stress. In addition the present model also emphasizes the isotropic hardening aspect through (13) and (14). These two material functions h_a and h_c are allowed to be functions of $\bar{e}^p$, which, as specified at the beginning in Section 2, may characterize the expansion/contraction of the yield surface. It is well known that the isotropic hardening contribution is very important for the task of modeling the cyclic behavior of materials, especially the nonproportional cyclic loading ones.

4. Weak stability criteria

The substitution of Equations (3) and (4) into the inner product of Gs^a_{ij} with (1) gives

$$Gs^a_{ij}\dot{e}_{ij} = \frac{1}{2}s^a_{ij}\dot{s}_{ij} + \frac{3G\dot{\lambda}_a}{2h_a}s^a_{ij}s^a_{ij} + \frac{3G\dot{\lambda}_c}{2h_c}s^a_{ij}s^c_{ij}. \tag{26}$$

The plastic modulus E_p is defined by [Dafalias 1984]

$$\dot{e}^p_{ij} = \frac{n_{kl}\dot{s}_{kl}}{\frac{2}{3}E_p}\nu_{ij}, \tag{27}$$

where ν_{ij} is the unit normal direction of the plastic strain rate, and

$$n_{ij} := \frac{1}{\| \frac{\partial f_a}{\partial s_{ij}} \|}\frac{\partial f_a}{\partial s_{ij}} = \frac{1}{\sqrt{\frac{2}{3}}h_a}s^a_{ij} \tag{28}$$

is the unit normal direction of the yield surface, which can be deduced from Equation (13). Substituting (28) into (27) gives

$$\dot{e}^p_{ij} = \frac{3s^a_{kl}\dot{s}_{kl}}{2\sqrt{\frac{2}{3}}E_p h_a}\nu_{ij}.$$

The substitution of the above equation into (15) further leads to

$$s_{ij}^a \dot{s}_{ij} = \frac{2}{3} E_p h_a \dot{\bar{e}}^p. \tag{29}$$

If both the yield and contact conditions are satisfied, by using (29) and (26) we have

$$3G s_{ij}^a \dot{e}_{ij} = E_p h_a \dot{\bar{e}}^p + 3G h_a \dot{\lambda}_a + \frac{9G}{2h_c} \dot{\lambda}_c s_{ij}^a s_{ij}^c. \tag{30}$$

By inserting the plastic flow rule (4) into (15), it follows that

$$\dot{\lambda}_a^2 + \frac{3\dot{\lambda}_c s_{ij}^a s_{ij}^c}{h_a h_c} \dot{\lambda}_a + \dot{\lambda}_c^2 - (\dot{\bar{e}}^p)^2 = 0.$$

Then, by using (16) and (17) we can derive the following result:

$$\dot{\lambda}_a = \gamma_a \dot{\bar{e}}^p, \tag{31}$$

where

$$\gamma_a := -\gamma_c \left(\gamma_c + \frac{h_c'}{k_c'}\right) + \sqrt{\left(\gamma_c^2 + \gamma_c \frac{h_c'}{k_c'}\right)^2 + 1 - \gamma_c^2}. \tag{32}$$

If $0 \le \gamma_c < 1$ (see below), it is easy to prove that

$$\gamma_a > 0. \tag{33}$$

If the second switch is in the *off* state, that is, $\dot{\lambda}_c = 0$, we have $\gamma_c = 0$ by Equation (16). Thus $\gamma_a = 1$ via (32), and simultaneously Equation (31) reduces to

$$\dot{\lambda}_a = \dot{\bar{e}}^p. \tag{34}$$

Hence, once the term $\dot{\bar{e}}^p$ in (30) is replaced by $\dot{\lambda}_a$, we can obtain

$$3G s_{ij}^a \dot{e}_{ij} = (E_p + 3G) h_a \dot{\lambda}_a. \tag{35}$$

For the case of $\dot{\lambda}_c > 0$, from Equations (30), (31), (32), (16) and (17) it follows that

$$3G s_{ij}^a \dot{e}_{ij} = \left(E_p + 3G \sqrt{\left(\gamma_c^2 + \gamma_c \frac{h_c'}{k_c'}\right)^2 + 1 - \gamma_c^2}\ \right) h_a \dot{\bar{e}}^p, \tag{36}$$

which reduces to Equation (35), when $\gamma_c = 0$.

The following inequality can be proved:

$$\left(\gamma_c^2 + \gamma_c \frac{h_c'}{k_c'}\right)^2 - \gamma_c^2 \le 0. \tag{37}$$

Since $s_{ij}^c / (\sqrt{\frac{2}{3}} h_c)$ and $s_{ij}^a / (\sqrt{\frac{2}{3}} h_a)$ are two unit tensors, from (17), (23), (11) and (15) it follows that

$$0 \le \gamma_c \le 1 - \frac{h_c'}{k_c'}, \quad \left(\gamma_c + \frac{h_c'}{k_c'}\right)^2 \le 1. \tag{38}$$

Then, by using

$$\left(\gamma_c^2+\gamma_c\frac{h_c'}{k_c'}\right)^2-\gamma_c^2=\left(\left(\gamma_c+\frac{h_c'}{k_c'}\right)^2-1\right)\gamma_c^2,$$

the inequality (37) is proved. From this result we have

$$E_p+3G\sqrt{\left(\gamma_c^2+\gamma_c\frac{h_c'}{k_c'}\right)^2+1-\gamma_c^2}\le E_p+3G. \tag{39}$$

The above equality holds only for $\gamma_c=0$ or $\gamma_c=1-h_c'/k_c'$, which, in view of (32), corresponds to $\gamma_a=1$ or $\gamma_a=h_c'/k_c'$. For these two cases, we have $\gamma_a+\gamma_c=1$. But from (17) with $\gamma_c=1-h_c'/k_c'$, we have $s_{ij}^a s_{ij}^c=2h_a h_c/3$, which is substituted into (19), and then the use of yield and contact conditions leads to $\mathcal{D}=0$. Thus from (18) we have $h_c'/k_c'=1$, which makes $\gamma_c=0$ and $\gamma_a=1$ again. So the range of γ_c in (38) is modified to

$$0\le\gamma_c<1-\frac{h_c'}{k_c'}. \tag{40}$$

The range of γ_c can be estimated more precisely. From Equation (18) we have $k_c'\ge h_c'$ and thus, by (23),

$$0<\frac{h_c'}{k_c'}\le 1. \tag{41}$$

From (40) it follows that

$$0\le\gamma_c<1.$$

In summary, $\gamma_a+\gamma_c=1$ holds only under the condition $\gamma_c=0$, and the equality in (39) holds only for the case of $\gamma_c=0$.

For other cases with the range of γ_c specified by (40) we can prove that

$$\gamma_a+\gamma_c\ge 1. \tag{42}$$

Inserting (32) for γ_a, the above inequality means that

$$\gamma_c-\gamma_c\left(\gamma_c+\frac{h_c'}{k_c'}\right)+\sqrt{\left(\gamma_c^2+\gamma_c\frac{h_c'}{k_c'}\right)^2+1-\gamma_c^2}\ge 1.$$

Thus, we have

$$0<1-\gamma_c+\gamma_c\left(\gamma_c+\frac{h_c'}{k_c'}\right)\le\sqrt{\left(\gamma_c^2+\gamma_c\frac{h_c'}{k_c'}\right)^2+1-\gamma_c^2}. \tag{43}$$

To prove the first inequality in the above, that is,

$$\gamma_c^2+\left(\frac{h_c'}{k_c'}-1\right)\gamma_c+1>0,$$

let us note that the above inequality holds when $\gamma_c=0$ and that the discriminant satisfies

$$\left(\frac{h_c'}{k_c'}-1\right)^2-4<0$$

by (41). Therefore, the first inequality in Equation (43) follows obviously.

Taking the square of both the sides and canceling the common terms of the second inequality in (43), we obtain

$$\gamma_c\left(\gamma_c+\frac{h_c'}{k_c'}-1\right)\le 0.$$

It is true for γ_c in the range specified by (40). Thus the inequality in (42) is proved.

As discussed above, the equality $\gamma_a+\gamma_c=1$ holds only under the condition $\gamma_c=0$, and for the other cases of $\gamma_c>0$, we always have $\gamma_a+\gamma_c>1$, which, together with the plastic flow rule in equation (4) and (16) and (31), indicates that the plastic flow increases under the condition of contact. Indeed, $\dot{\bar{e}}^p$ is a quantity to measure the strength of plastic flow. When comparing (35) and (36) and noting the inequality (39), we can also conclude that the plastic flow under the condition of contact is stronger than that in the noncontact condition.

Under the condition $\dot\lambda_c=0$, the weak stability criteria are

$$G>0,\qquad h_a>0,\qquad E_p+3G>0. \tag{44}$$

Otherwise, under the condition of $\dot\lambda_c>0$, the weak stability criteria are

$$G>0,\ h_a>0,\ E_p+3G\sqrt{\left(\gamma_c^2+\gamma_c\frac{h_c'}{k_c'}\right)^2+1-\gamma_c^2}>0. \tag{45}$$

If $f_a=0$, the consistency condition reads as

$$\frac{\partial f_a}{\partial s_{ij}^a}\dot s_{ij}^a+\frac{\partial f_a}{\partial \bar e^p}\dot{\bar e}^p=0,$$

or by Equation (13), further reads as

$$s_{ij}^a\dot s_{ij}^a=\frac{2}{3}h_a h_a'\dot{\bar e}^p. \tag{46}$$

Then, taking the inner product of both the sides of (4) with s_{ij}^a with the help of (31), (16) and (17) leads to

$$s_{ij}^a\dot e_{ij}^p=\left(\gamma_a+\gamma_c\left(\gamma_c+\frac{h_c'}{k_c'}\right)\right)h_a\dot{\bar e}^p. \tag{47}$$

This equation is to be used later.

5. Switch of plastic irreversibility

The first complementary trio (7)–(9) enables the model to possess a switch of plastic irreversibility, whose *on/off* conditions are derived below.

We first consider the case of $\dot\lambda_c=0$. If the yield condition $f_a=0$ and the consistency condition $\dot f_a=0$ are satisfied, but the contact condition is unsatisfied, that is, $f_c<0$ and thus $\dot\lambda_c=0$ by (12), then (35) can be used. Because of (44) for the weak stability criteria of the case of $\dot\lambda_c=0$, from Equation (35) it follows that

$$\text{if } f_a=0,\quad \text{then}\quad s_{ij}^a\dot e_{ij}>0\Longleftrightarrow\dot\lambda_a>0. \tag{48}$$

Thus, we have

$$f_a=0\quad\text{and}\quad s_{ij}^a\dot e_{ij}>0\Rightarrow\dot\lambda_a>0. \tag{49}$$

On the other hand, if $\dot{\lambda}_a > 0$, (9) ensures $f_a = 0$, which, together with (48), asserts that

$$\dot{\lambda}_a > 0 \Rightarrow f_a = 0 \quad \text{and} \quad s^a_{ij}\dot{e}_{ij} > 0. \tag{50}$$

Therefore, from (49) and (50) we conclude that the yield condition $f_a = 0$ and the straining condition $s^a_{ij}\dot{e}_{ij} > 0$ are sufficient and necessary for plastic irreversibility with $\dot{\lambda}_a > 0$. Considering this and Equation (7), we thus possess the following switching criteria of plastic irreversibility:

$$\dot{\lambda}_a \begin{cases} > 0, & \text{if } f_a = 0 \quad \text{and} \quad s^a_{ij}\dot{e}_{ij} > 0, \\ = 0, & \text{if } f_a < 0 \quad \text{or} \quad s^a_{ij}\dot{e}_{ij} \le 0, \end{cases} \tag{51}$$

or, due to Equations (31) and (33),

$$\dot{\bar{e}}^p \begin{cases} > 0, & \text{if } f_a = 0 \quad \text{and} \quad s^a_{ij}\dot{e}_{ij} > 0, \\ = 0, & \text{if } f_a < 0 \quad \text{or} \quad s^a_{ij}\dot{e}_{ij} \le 0. \end{cases} \tag{52}$$

Next, we consider the case of $\dot{\lambda}_c > 0$, from which we have (36). Because of (45) for the weak stability criteria of the case of $\dot{\lambda}_c > 0$, from (36) it follows that

$$\text{if } f_a = 0, \quad \text{then} \quad s^a_{ij}\dot{e}_{ij} > 0 \Longleftrightarrow \dot{\bar{e}}^p > 0. \tag{53}$$

Thus,

$$f_a = 0 \quad \text{and} \quad s^a_{ij}\dot{e}_{ij} > 0 \Rightarrow \dot{\bar{e}}^p > 0. \tag{54}$$

On the other hand, if $\dot{\bar{e}}^p > 0$, then $\dot{\lambda}_a > 0$ by (31) and (33), and then (9) assures $f_a = 0$, which, together with (36), asserts that

$$\dot{\bar{e}}^p > 0 \Rightarrow f_a = 0 \quad \text{and} \quad s^a_{ij}\dot{e}_{ij} > 0.$$

Therefore, from Equations (53) and (54) we conclude that the yield condition $f_a = 0$ and the straining condition $s^a_{ij}\dot{e}_{ij} > 0$ are sufficient and necessary for the plastic irreversibility with $\dot{\bar{e}}^p > 0$. For this case, we thus possess the same switching criteria of plastic irreversibility as that given by Equation (52).

In the *on* state of the switch, $\dot{\lambda}_a > 0$ and $\dot{\bar{e}}^p > 0$, the mechanism of plastic irreversibility is working and the material exhibits elastoplastic behavior, while in the *off* state of the switch, $\dot{\lambda}_a = 0$ and $\dot{\bar{e}}^p = 0$, the material is reversible and elastic. According to the complementary trio (7)–(9), there are two states: (i) $\dot{\lambda}_a > 0$ and $f_a = 0$, and (ii) $\dot{\lambda}_a = 0$ and $f_a \le 0$. From the switch (51) it is clear that (i) corresponds to the *on* state whereas (ii) corresponds to the *off* state.

6. Switch of kinematic hardening rules

The following discussion is under the condition of $\dot{\bar{e}}^p > 0$ in the plastic state. The second complementary trio (10)–(12) enables the model to possess a switch of kinematic hardening rules, the *on/off* conditions of which are derived below.

If the contact condition $f_c = 0$ is not satisfied, that is, $f_c < 0$, then by Equation (12) we have $\dot{\lambda}_c = 0$ and then $\gamma_c = 0$ by (16). Thus, before the occurrence of contact from (6) we have

$$\dot{s}^c_{ij} = \frac{2}{3}k'_c\dot{e}^p_{ij}. \tag{55}$$

Continuously moving under the above governing law of contact stress, the contact may happen, that is, $f_c = 0$, because of $k_c' > 0$ by (23), and at the moment of contact, if $\dot{f}_c > 0$, there will eventually occur a penetration to violate the contact condition. From (14) and (55) the penetration condition can be derived as follows:

$$k_c' s_{ij}^c \dot{e}_{ij}^p - h_c h_c' \dot{\bar{e}}^p > 0.$$

The substitution of (4) and (34) into the above equation gives

$$\left(\frac{3}{2h_a} k_c' s_{ij}^c s_{ij}^a - h_c h_c'\right)\dot{\bar{e}}^p > 0.$$

Due to (23), dividing the above equation by $h_c k_c' > 0$, leads to

$$\left(\frac{s_{ij}^c}{\sqrt{\frac{2}{3}}h_c}\frac{s_{ij}^a}{\sqrt{\frac{2}{3}}h_a} - \frac{h_c'}{k_c'}\right)\dot{\bar{e}}^p = \gamma_c \dot{\bar{e}}^p > 0,$$

where the definition given in Equation (17) is used. Using the definition (16) the penetration condition now reads as

$$f_c = 0 \qquad \text{and} \qquad \dot{\lambda}_c > 0. \tag{56}$$

Therefore, upon happening the contact we cannot continuously use (55) to avoid the penetration, and the contact law must be switched to (6).

Considering this and (10), we thus possess the following switching criteria of kinematic hardening rules:

$$\dot{\lambda}_c \begin{cases} > 0, & \text{if} \quad f_c = 0 \quad \text{and} \quad \gamma_c > 0, \\ = 0, & \text{if} \quad f_c < 0 \quad \text{or} \quad \gamma_c = 0. \end{cases} \tag{57}$$

In the *on* state of the switch, $\dot{\lambda}_c > 0$, the mechanism of kinematic hardening is working according to (24), while in the *off* state of the switch, $\dot{\lambda}_c = 0$, the kinematic hardening rule is still governed by (24) but with $\dot{\lambda}_c = 0$ and $\gamma_c = 0$, that is, the Prager kinematic hardening rule:

$$\dot{s}_{ij}^b = \frac{2}{3} k_a' \dot{e}_{ij}^p. \tag{58}$$

According to the complementary trio (10)–(12), there are two states of the kinematic hardening: (i) $\dot{\lambda}_c > 0$ and $f_c = 0$, and (ii) $\dot{\lambda}_c = 0$ and $f_c \le 0$. From the switch (57) it is clear that (i) corresponds to the *on* state whereas (ii) to the *off* state.

7. The coefficient functions

The existence of contact surface will affect the motion of yield surface, and thus the kinematic hardening rules must be modified to abide the contact rule. In contrast to the penetration condition as given in (56), the nonpenetration condition is

$$(f_c < 0) \quad \text{or} \quad (f_c = 0 \text{ and } \dot{f}_c \le 0). \tag{59}$$

The condition of $f_c < 0$ corresponds to the *off* state of the second switch. In the rest of this section, we will consider the case of *on* state of the switch of (57), that is, $\dot{\lambda}_c > 0$. By Equation (14), the conditions

of $f_c = 0$ and $\dot{f}_c \le 0$ in the above can be written as

$$\frac{3}{2}s_{ij}^c s_{ij}^c = h_c^2,\ \ \frac{3}{2}s_{ij}^c \dot{s}_{ij}^c - h_c h_c' \dot{\bar{e}}^p \le 0. \tag{60}$$

This indeed supplies a constraint on the contact rule (6) in the case of $\dot{\lambda}_c > 0$.

Substitution of (6) into the latter one of (60) and the use of the former one lead to

$$-C_1 \dot{\lambda}_c h_c^2 + \Big(k_c' + \frac{3}{2}\gamma_c C_2\Big)s_{ij}^c \dot{e}_{ij}^p + \frac{3}{2}\gamma_c s_{ij}^c \dot{s}_{ij} \le h_c h_c' \dot{\bar{e}}^p. \tag{61}$$

Inserting

$$\gamma_c C_2 = -\frac{2}{3}k_c' \tag{62}$$

into (61), which, dividing by $\dot{\lambda}_c h_c^2$ and then using (23), (16) and $\dot{\lambda}_c > 0$, gives the following inequality

$$C_1 \ge \frac{3 s_{ij}^c \dot{s}_{ij}}{2h_c^2 \dot{\bar{e}}^p} - \frac{h_c'}{\gamma_c h_c}.$$

So we let

$$C_1 = \frac{3 s_{ij}^c \dot{s}_{ij}}{2h_c^2 \dot{\bar{e}}^p} - \frac{h_c'}{\gamma_c h_c} \tag{63}$$

to guarantee that the contact can be continued to avoid the penetration. By using (63) and (62) for C_1 and C_2, Equation (6) can be simplified to

$$\dot{s}_{ij}^c = \frac{h_c' \dot{\bar{e}}^p}{h_c} s_{ij}^c + \gamma_c \Big(\dot{s}_{ij} - \frac{3\dot{s}_{mn} s_{mn}^c}{2h_c^2} s_{ij}^c\Big). \tag{64}$$

Substituting Equations (5) and (62) into (46) leads to

$$-C_1 \dot{\lambda}_c s_{ij}^a s_{ij}^a - \frac{2}{3}(k_a' - k_c')s_{ij}^a \dot{e}_{ij}^p - C_3 \dot{\lambda}_c s_{ij}^a e_{ij}^p + (1-\gamma_c)s_{ij}^a \dot{s}_{ij} + C_4 \dot{\lambda}_c s_{ij}^a s_{ij} = \frac{2}{3}h_a h_a' \dot{\bar{e}}^p. \tag{65}$$

From Equations (16), (29), (47) and $f_a = 0$, the final form of the above equation can be obtained,

$$\gamma_c C_3 s_{ij}^a e_{ij}^p = \frac{2}{3}E_p h_a (1-\gamma_c) - \frac{2}{3}h_a \left\{h_a' + (k_a' - k_c')\Big(\gamma_a + \gamma_c\Big(\gamma_c + \frac{h_c'}{k_c'}\Big)\Big)\right\}$$
$$+\gamma_c C_4 s_{ij}^a s_{ij} - \gamma_c C_1 \frac{2h_a^2}{3}. \tag{66}$$

Up to now, there have been three equations (62), (63) and (66) to determine the four unknown coefficients C_1, C_2, C_3 and C_4. For simplicity, the remaining one is assumed to be

$$C_4 = \frac{-C_3}{2G}. \tag{67}$$

Substituting Equation (67) into (66) leads to

$$\gamma_c C_3 s_{ij}^a [e_{ij}^p + \frac{1}{2G}s_{ij}] = \frac{2}{3}E_p h_a (1-\gamma_c) - \gamma_c C_1 \frac{2h_a^2}{3} - \frac{2}{3}h_a \Big(h_a' + (k_a' - k_c')\Big(\gamma_a + \gamma_c\Big(\gamma_c + \frac{h_c'}{k_c'}\Big)\Big)\Big). \tag{68}$$

This equation can be used to determine C_3.

In summary, the procedures to obtain the coefficient functions are:

$$C_1 \text{ given by (63)} \longrightarrow C_3 \text{ from (68)} \longrightarrow C_4 \text{ from (67)} \longrightarrow C_2 \text{ from (62)}.$$

Under the noncontact condition, the governing equations of back stress and contact stress as presented by (58) and (55), respectively, have the same simpler form. However, under the contact condition, the governing equation of back stress becomes very complex, as shown by (24) with the above coefficient functions $C_1, \ldots, C_4$, whereas we can appreciate the neatness of the governing equation for the contact stress as shown by (64). Therefore, in terms of the concept of contact stress we can more precisely derive the contact condition and its switching criteria.

8. Plastic modulus

The equality of $\gamma_c = 0$ can happen for $\dot{\lambda}_c = 0$ in the *off* state of the switch (57), or for a state of which the yield surface is in contact with the bounding surface and stress is impinging simultaneously on the both surfaces. In this latter case the two unit tensors in (17) are in parallel, and thus, one has

$$\frac{s^c_{ij}}{\sqrt{\frac{2}{3}}h_c}\frac{s^a_{ij}}{\sqrt{\frac{2}{3}}h_a} = 1 \Rightarrow \gamma_c = 1 - \frac{h'_c}{k'_c}. \tag{69}$$

From (19) it is also $\mathcal{D} = 0$ for this case, and hence we have $h'_c/k'_c = 1$ in view of (18). So γ_c is zero by (69), and then $\dot{\lambda}_c = 0$ by (16). Therefore we have the same kinematic hardening rule as the one that is using before the occurrence of contact.

For the case of $\mathcal{D} = 0$ the plastic modulus $E_p = h'_a + k'_a$ is the slope of the stress-plastic strain curve in the uniaxial tension test after the intersection of the yield curve and the bounding curve. On the other hand, for the case of $\mathcal{D} > 0$ the plastic modulus $E_p = h'_a + k'_a$ is a function of h'_0, k'_0, $h_c = h_0 - h_a$ and $\mathcal{D}$, the last term of which is the distance between the current stress point and its image point on the bounding surface as shown by (19), and h'_0, k'_0, h_0, h_a are material functions, such that

$$E_p = h'_a + k'_a = (h'_0 + k'_0)\exp\Big(a\Big(\frac{\mathcal{D}}{2h_c}\Big)^b\Big). \tag{70}$$

The contact stress bound is given by $h_c = h_0 - h_a$ and the kinematic modulus of contact surface is given by $k'_c = k'_a - k'_0$. They are consistent with (18). It means that (70) is a direct result of (18) by inserting $h'_c = h'_0 - h'_a$ and $k'_c = k'_a - k'_0$.

The substitution of (70) into (35) gives

$$\dot{\bar{e}}^p = \frac{3Gs^a_{ij}\dot{e}_{ij}}{h_a\Big((h'_0 + k'_0)\exp\big(a\big(\frac{\mathcal{D}}{2h_c}\big)^b\big) + 3G\Big)}, \tag{71}$$

from which the amount of $\dot{\bar{e}}^p$ can be greatly reduced for a larger $\mathcal{D} > 0$. This result can be compared with that demonstrated in Section 4, where the plastic flow increases under the condition of contact.

When the yield surface is in contact with the bounding surface and stress stands on both surfaces, we have $\mathcal{D} = 0$, and thus from (70) we have $h'_a + k'_a = h'_0 + k'_0$, which guarantees the continuity of plastic modulus.

9. Experimental tests of SAE 4340 and RHA

In this section the materials SAE 4340 and RHA (rolling homogeneous armory) under various loadings in an MTS axial-torsional test system are investigated. The investigation includes loading, unloading, reverse loading, and cyclic loading for uniaxial and biaxial conditions. The related basic material functions used in the constitutive laws are identified based on the experimental data.

The conventional method to obtain the material functions in the classic plasticity models is to perform the uniaxial tension/compression or torsional test. These techniques seem to be sufficient to fit the material functions of mixed-hardening model only, and not enough to fit the material functions needed in the constitutive equations of the present paper for a more powerful cyclic model. The other drawback of a simple test is that the range of equivalent plastic strain $\bar{e}^p$ is too small (about 10 percent), such that the material functions obtained from that test may not be appropriate for the cyclic loading conditions, because the value of $\bar{e}^p$ may reach over 100% in a typical cyclic loading test.

9.1. *Experimental method.*

Experimental apparatus and method. For the uniaxial tension/compression cyclic test the results can be used to determine the material functions used in the constitutive equations. For this purpose a uniaxial cyclic test is designed, which is conducted in the MTS test system under strain control.

The biaxial cyclic loading test was conducted with an MTS 458.20 Axial-Torsional test machine of the College of Engineering of the National Taiwan University. This machine can be feedback controlled simultaneously for axial and torsional directions by either stroke, load or strain control.

In this series of tests the strain control mode was selected, which is the most stable control method. The measurement of strain was performed by the MTS 632.80C-04 biaxial extensometer.

A thin-walled tube was adopted as the test specimen. When the ratio of outside diameter to thickness is large enough (about 8/1), the stress $(\sigma_{11}, \sigma_{12})$ can be viewed as uniformly distributed in the axial parallel portion of the specimen.

Size and material of specimen. We chose two metallic materials to be tested, the chemical compositions of which are shown in Table 1.

The size of the specimen for the uniaxial test was of total length 12 cm, the end parts with length 4 cm and diameter 16 mm, and the parallel portion with length greater than 3 cm and diameter 8 mm. The uniaxial extensometer MTS 623.11C-20 was used to measure strain.

The gauge length of the biaxial extensometer MTS 632.80C-04 was 25 mm. Therefore, the outside diameter of the parallel portion of the specimen was restricted to 25 mm, and the end part was 46 mm. The inside diameter of the parallel part of the specimen was chosen to be 23 mm, so the outside diameter/thickness ratio was less than 8/1 to avoid the buckling of the specimen under compression.

	C	Mn	P	S	Si	Cr	Ni	Mo	Al
SAE 4340	0.3746	0.6196	0.0177	0.0168	0.2116	0.6344	1.592	0.1584	0.0256
RHA	0.2413	0.2128	0.0114	0.0140	0.2171	1.160	2.851	0.2499	0.0197

Table 1. Chemical compositions of tested materials.

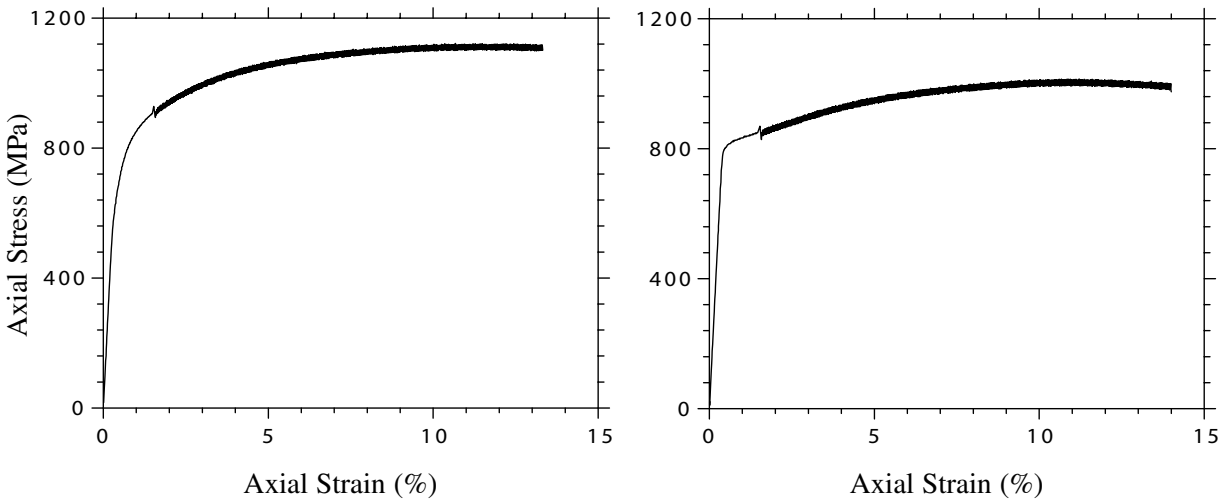

Figure 2. Experimental results of (left) SAE 4340 and (right) RHA under monotonic axial strain.

9.2. ***Experimental path design.*** Metallic materials in general exhibit hardening and then softening in the stress-strain curve for the uniaxial monotonic loading test. Because the stress control experiment cannot be conducted in the range of softening, the experiments are all of the strain-controlled tests in this paper. Hence, the ratcheting effects which can be revealed only in the stress-controlled tests were not studied in this paper.

The following strain paths likely to occur with a typical structure during repeated loadings were chosen:

(1) Uniaxial experiments:

  (a) Monotonic axial loading from $\epsilon_{11} = 0$ to $\epsilon_{11} = 15\%$: Figure 2.
  (b) Cyclic loading

    (i) mean strain 0 and strain amplitude 1.5%: Figure 3.
    (ii) mean strain 1.5% and strain amplitude 1.5%: Figure 4.
    (iii) initial mean strain equals zero and initial strain amplitude equals 0.6%, and mean strain and strain amplitude are increased cyclically both with the amounts of 0.3% per each cycle up to the values of 1.8% for mean strain and 2.4% for strain amplitude: Figure 5.
    (iv) initial mean strain equals zero and initial strain amplitude equals 0.5%, and strain amplitude is increased cyclically with the amount of 0.5% per each cycle: Figure 6.

(2) Biaxial experiments:

  (a) Proportional cyclic loadings with different ratios: Figures 7 and 8.
  (b) Non-proportional cyclic loading with phase lags of 0°, 45°, 90° and 135°: Figures 9 and 10.
  (c) Square paths: Figures 11 and 12.

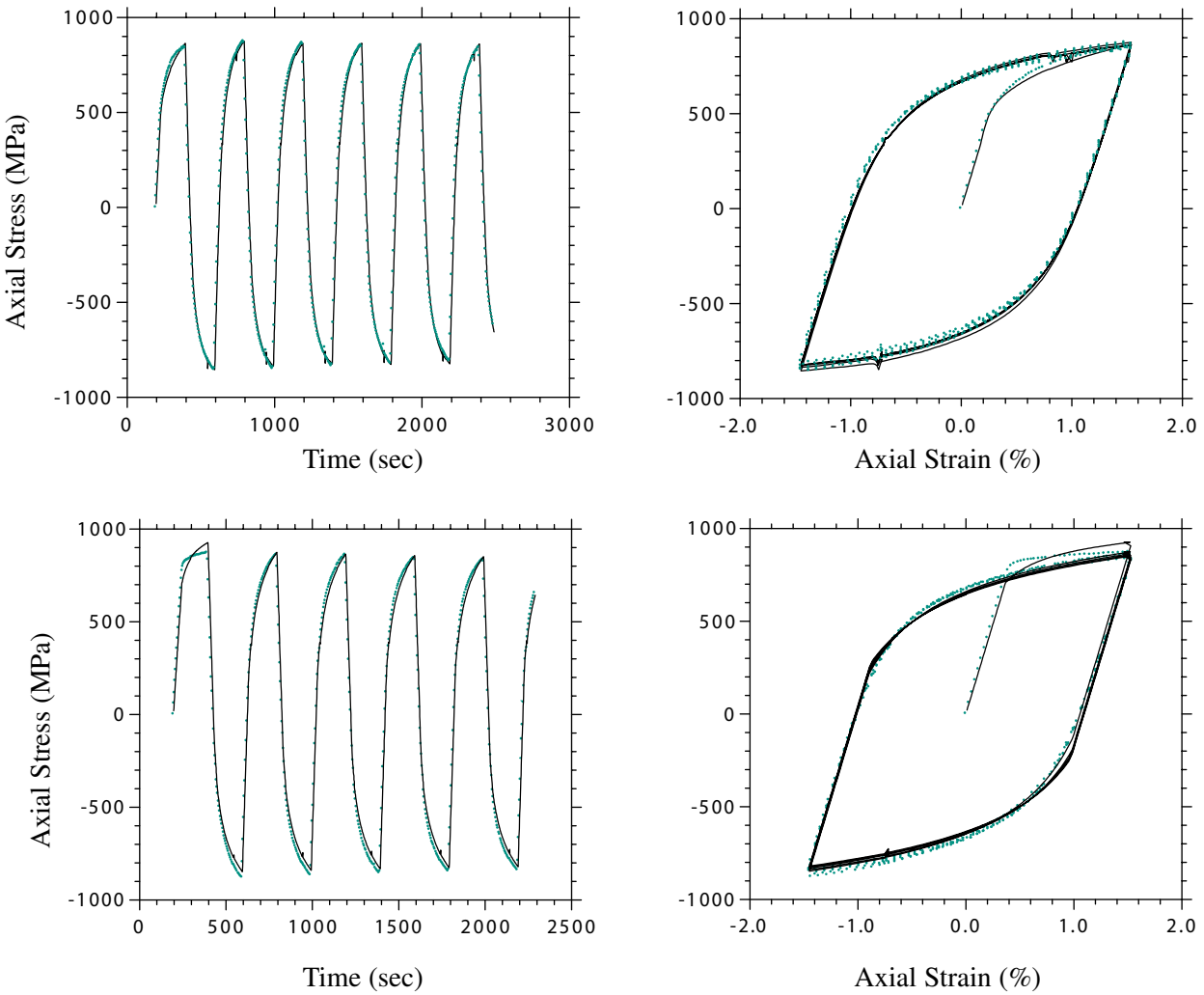

Figure 3. Experimental and simulated results for (top) SAE 4340 and (bottom) RHA under cyclic axial strain with amplitude 1.5% and zero mean. Left: time history of axial stress; right: axial stress versus axial strain. Green dots represent experimental values, solid lines represent the theory.

In the biaxial tests, each subpart was carried out for five cycles. All the tests were conducted at room temperature under a nearly quasistatic process (the axial strain rate was about $10^{-4}\mathrm{s}^{-1}$ and the shear strain rate was about $1.732 \times 10^{-4}\mathrm{s}^{-1}$). Thus the thermal effect and the rate effect were excluded.

All the stress-strain curves that appear in this paper were plotted by the computer from the acquired data without any data smoothing effort; some irregular bursts presented in the figures may be attributed to the electrical and hydraulic instability of the test machine. The discussions of the test results are given below.

9.3. *Experimental results.*

Uniaxial experiments. Figure 2 displays the stress-strain relation of SAE 4340 and RHA. The Young's modulus of SAE 4340 is about 200 GPa, and the yield point is detected at about 870 MPa. At a strain of 12%, SAE 4340 is hardened to 1100 MPa. The Young's modulus of RHA is about 200 GPa, and the yield point is detected at about 800 MPa. At a strain of 12%, RHA is hardened to 1000 MPa.

From Figure 3 it can be seen that the initial yield of SAE 4340 occurred at a stress equal to 600 MPa. When the reverse loading was applied up to the plastic range again the yield stress was reduced to −400 MPa, which is much less than the tensile stress. This phenomenon is known as the Bauschinger effect. After the second cycle, SAE 4340 displayed a cyclic softening and tended to saturation rather fast. Eventually, the maximum tensile stress 900 MPa and maximum compressive stress −850 MPa were reached with the strain amplitude of 1.5%. From this fact we know that the cyclic stress response is drastically different from the simple loading test. At this test, the Bauschinger and Masing effects are apparent. From Figure 3, it appears that the cyclic behavior of RHA is similar to that of SAE 4340.

Figure 4 shows the test results with mean strain different from zero. Since the mean of strain is not zero, the cyclic stress-strain curve shows a shift in the positive strain direction. Basically, the experimental result is similar to the above case, but in this case the stabilization of the cyclic curve is quicker than that of the previous loading case. This phenomenon may be attributed to the fact that the accumulated plastic strain is larger than that in Figure 3 before the cyclic loading is executed.

The purpose of the tests shown in Figure 5 is to investigate both the effects of strain amplitude and mean stress on the cyclic stress-strain curve. Both materials tested exhibited a mixed-hardening behavior. The right panels in these figures show the results due to the interaction of amplitude and mean, in which the elastic range is increased gradually, that is, the isotropic hardening increased with increasing amplitude and mean. In addition, the kinematic hardening seems saturated. It seems that the effect of the memory of maximum plastic strain can be investigated from this test.

The test results shown in Figure 6 can be used to investigate the influence of increasing strain amplitude. The expansion and contraction of the elastic range can be investigated, which means that the isotropic hardening and then softening occur in this test; on the other hand the kinematic hardening tends to saturation as shown in the right-hand panes of the figure. Due to the large strain amplitudes imposed in this test, it can be seen that the material hardens immensely, then softens slightly and then reaches towards a final failure only within a few cycles.

Biaxial experiments. The results of the biaxial experiments are shown in Figures 7 and 8, which plot the results of proportional loading tests with different ratios of axial strain amplitudes and shear strain amplitudes. In the first five cycles of the strain path with a zero shear strain, the stress-strain relations are similar to the results obtained from a uniaxial cyclic test. In the second stage the shear strain is raised by a ratio of half the amplitude of the axial strain. The hysteresis loop of axial stress-axial strain in this stage becomes smaller than that of the previous one due to the reduction of axial strain. In this stage the hysteresis loop seems saturated very soon to a stable shape. In the third stage the ratio of axial strain amplitude to shear strain amplitude is $2 : \sqrt{3}$, and the size of axial hysteresis loop becomes much smaller. At the fourth stage a pure shear imposed, the size of shear hysteresis loop increases and the axial stress relaxes. The fifth and sixth stages are the same as that of the third and second stages with only the axial strains being now inversed to a compressive one. In the last two stages further hardening is detected.

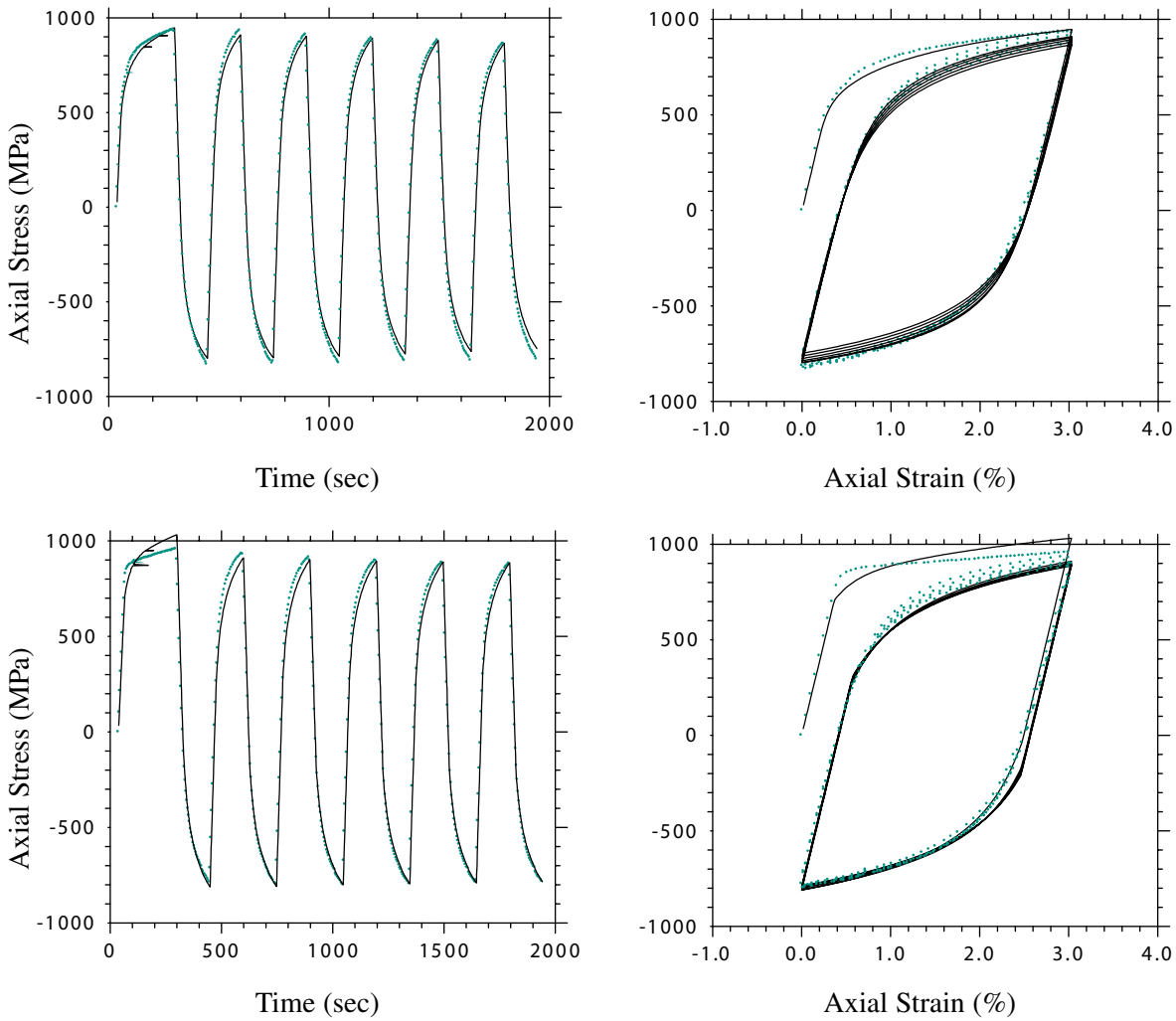

Figure 4. Experimental and simulated results of (top) SAE 4340 and (bottom) RHA under cyclic axial strain with amplitude 1.5% and mean 1.5%. Left: time history of axial stress; right: axial stress versus axial strain. Green dots represent experimental values, solid lines represent the theory.

Figures 9 and 10 show and compare the test results of nonproportional loadings with phase lags of 0°, 45°, 90° and 135°, respectively. In the first stage it is a proportional biaxial loading, in which the stress is reduced slightly as compared with the uniaxial test. In the second stage a 45° phase lag biaxial loading is applied. The hysteresis loops reveal a great distortion and hardening, and the stress path is displayed as an ellipse. The phase lag is increased to 90° in the third stage. More hardening phenomenon can be seen, the hysteresis loop looks like an ellipse, and the stress path looks like a circle. In the fourth stage the phase lag is 135°. The stress-strain diagrams are similar to the results in the previous stage with the roles of the two axes interchanged. No further hardening exists in this stage.

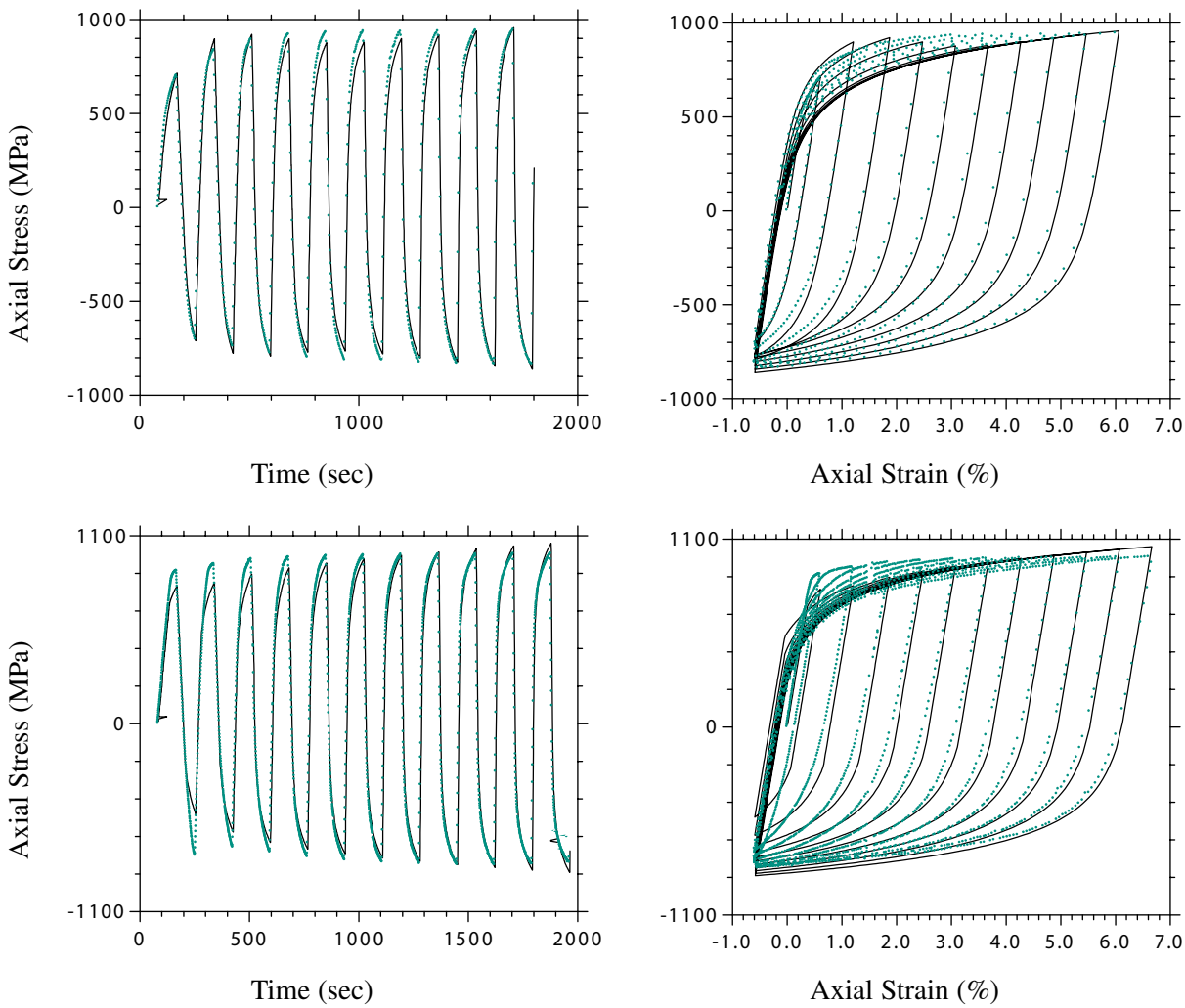

Figure 5. Experimental and simulated results for (top) SAE 4340 and (bottom) RHA under cyclic axial strain with increasing amplitude 0.6% per cycle and fixed compressive strain -0.6%. Left: time history of axial stress; right: axial stress versus axial strain. Green dots represent experimental values, solid lines represent the theory.

The experimental results given in Figures 11 and 12 are used to evaluate the alternative loading-unloading effects on the two materials tested. In the first stage which starts from a shear strain loading, an upper yield point can be seen. The strain hardening is apparent in this test. The stress relaxation to zero value and stablization appear when the strain is held in one direction. In the second stage, an over hardening phenomenon can be seen.

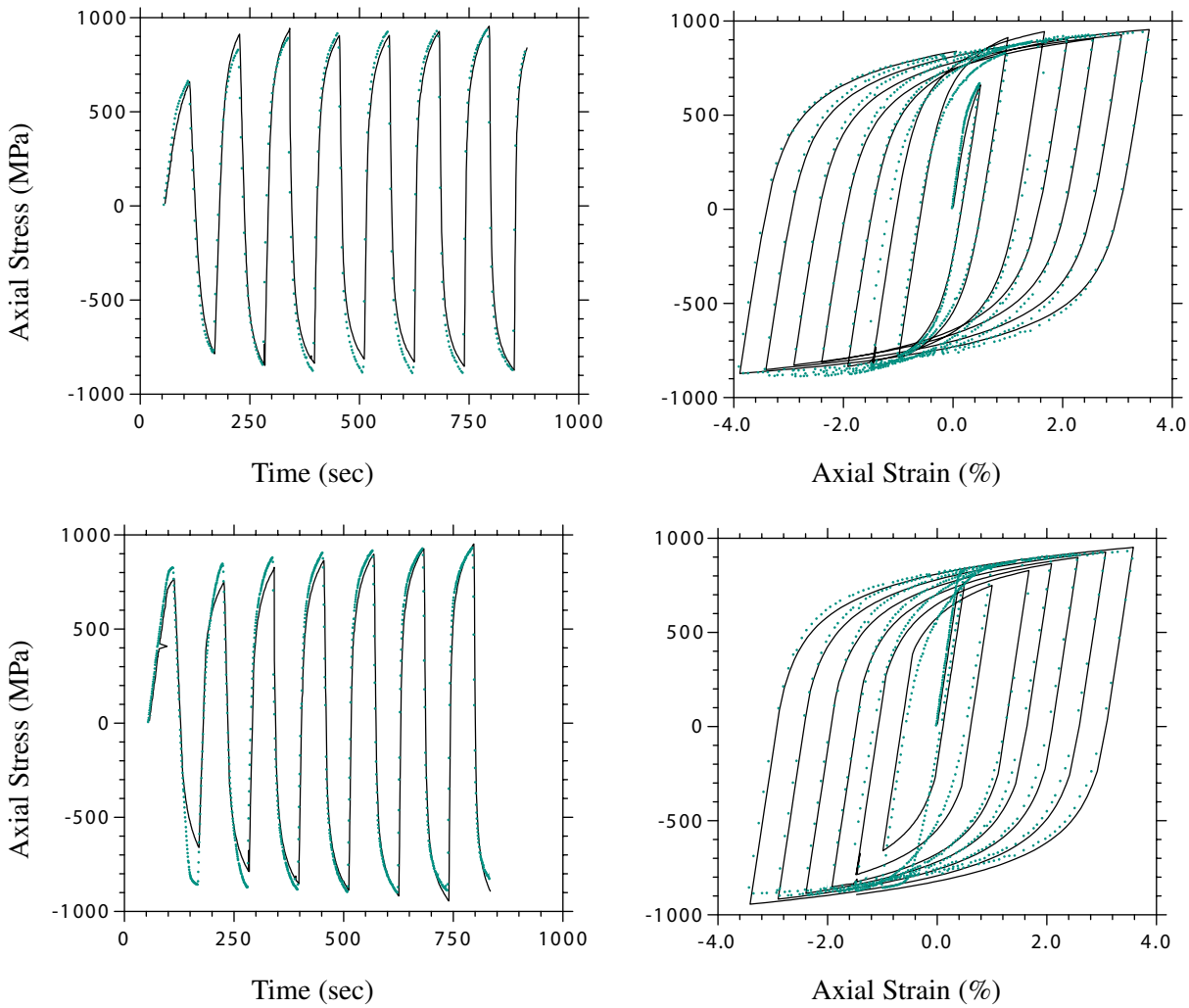

Figure 6. The experimental and simulated results of (top) SAE 4340 and (bottom) RHA under cyclic axial strain with increasing amplitude 0.5% per cycle but with zero mean. Left: time history of axial stress; right: axial stress versus axial strain. Green dots represent experimental values, solid lines represent the theory.

10. Discussion

In this experimental study, SAE 4340 and RHA were investigated under various uniaxial and biaxial cyclic loadings under strain control. Accordingly, the following results can be summarized.

(1) Precluding the thermal and rate effects, the reverse loading path abides the mixed hardening rules. In all tests the Bauschinger and Masing effects are apparent.

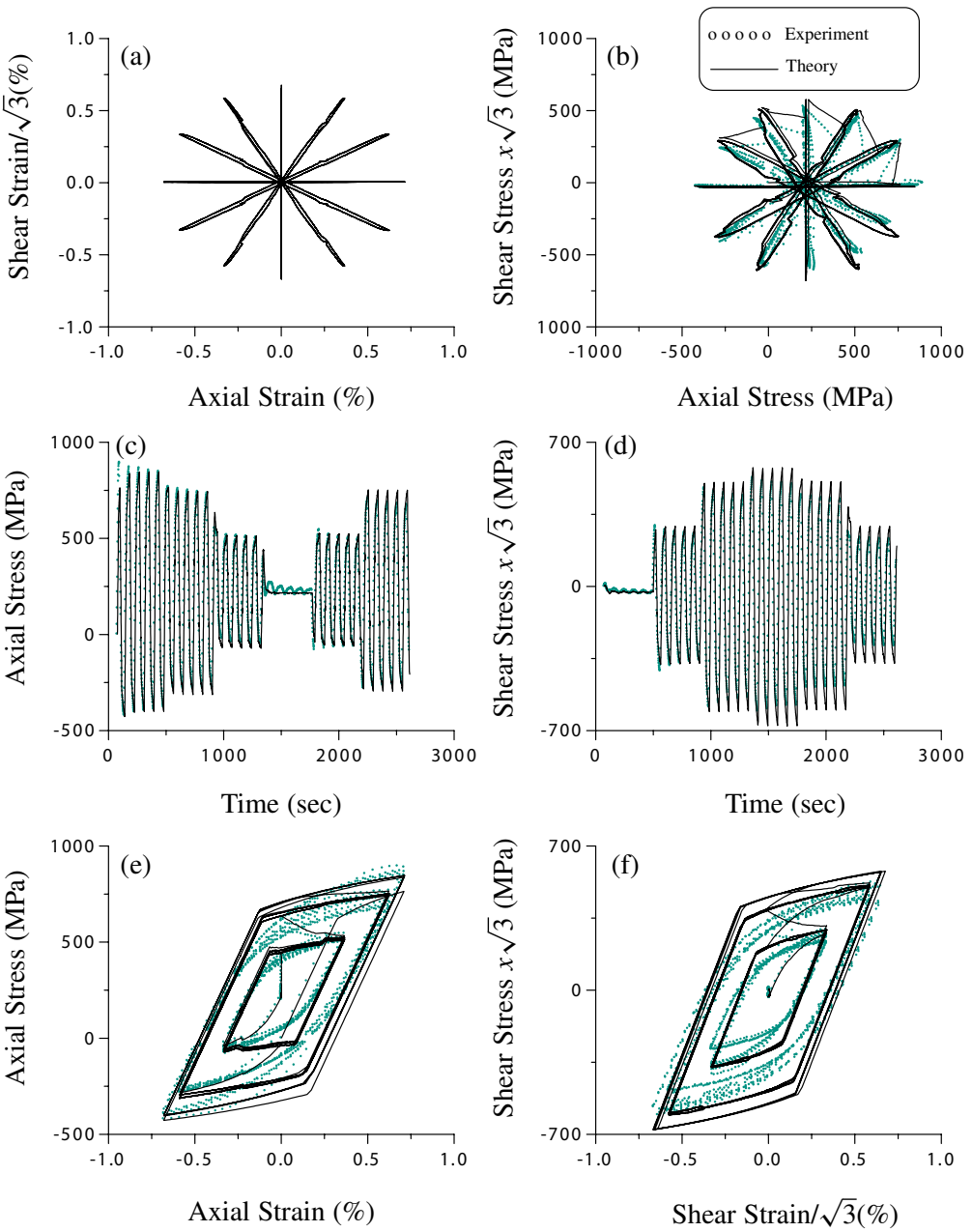

Figure 7. The experimental and simulated results of SAE 4340 under cyclic biaxial strain with input given in (a), and (b) the corresponding biaxial stress path, (c) time history of axial stress, (d) time history of shear stress, (e) axial stress versus axial strain, (f) shear stress versus shear strain.

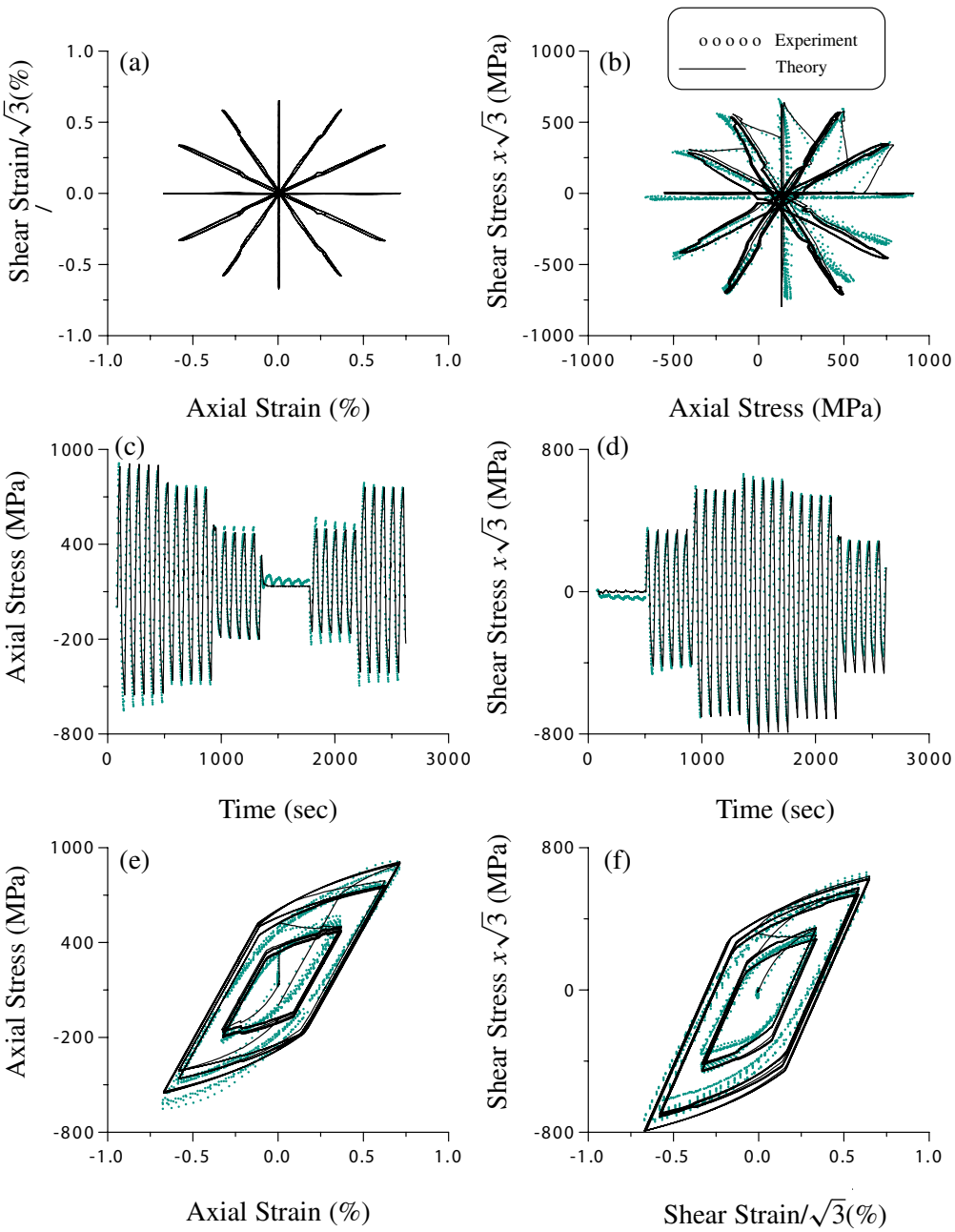

Figure 8. The experimental and simulated results of RHA under cyclic biaxial strain with input given in (a), and (b) the corresponding biaxial stress path, (c) time history of axial stress, (d) time history of shear stress, (e) axial stress versus axial strain, (f) shear stress versus shear strain.

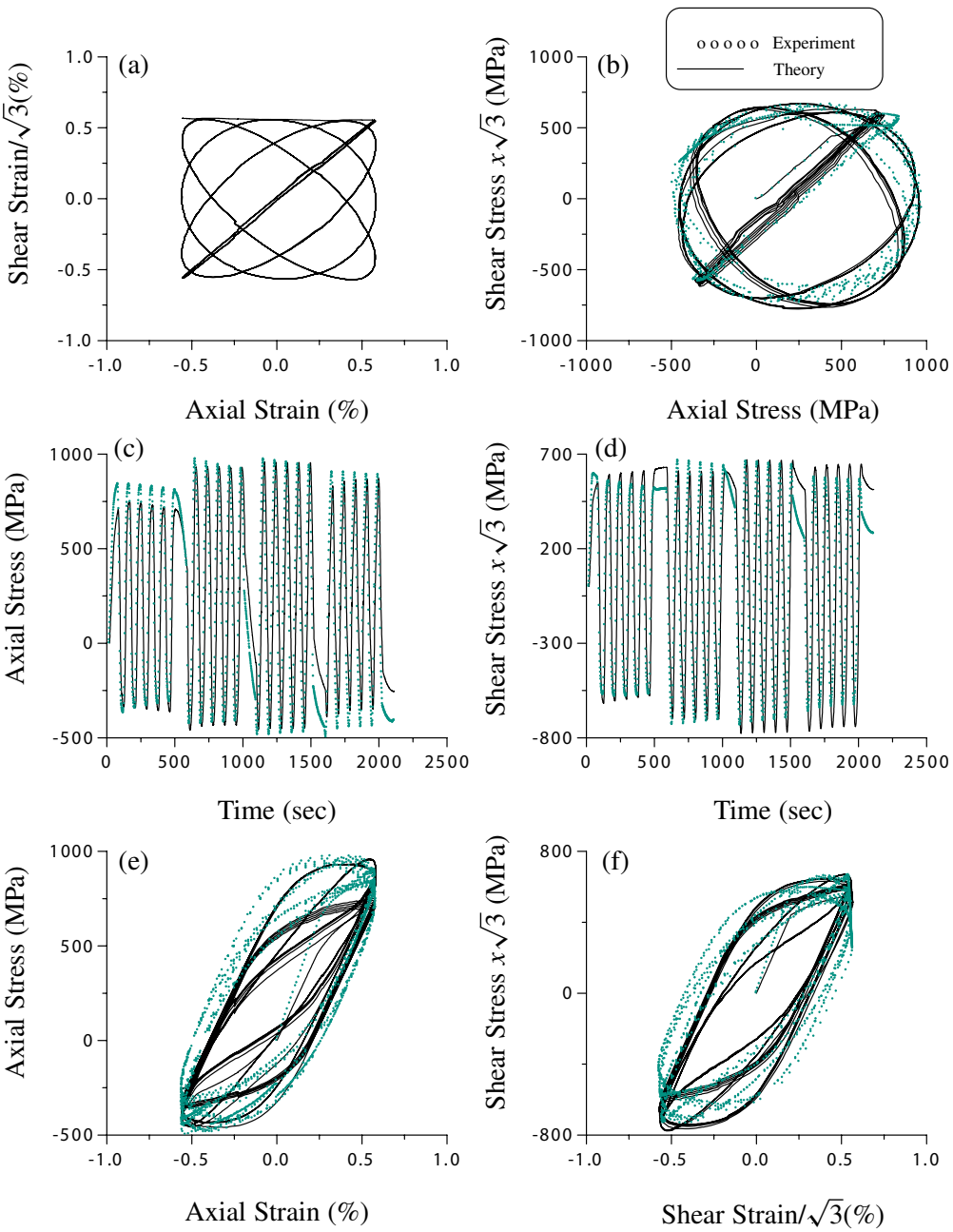

Figure 9. The experimental and simulated results of SAE 4340 under cyclic biaxial strain with input given in (a), and (b) the corresponding biaxial stress path, (c) time history of axial stress, (d) time history of shear stress, (e) axial stress versus axial strain, (f) shear stress versus shear strain.

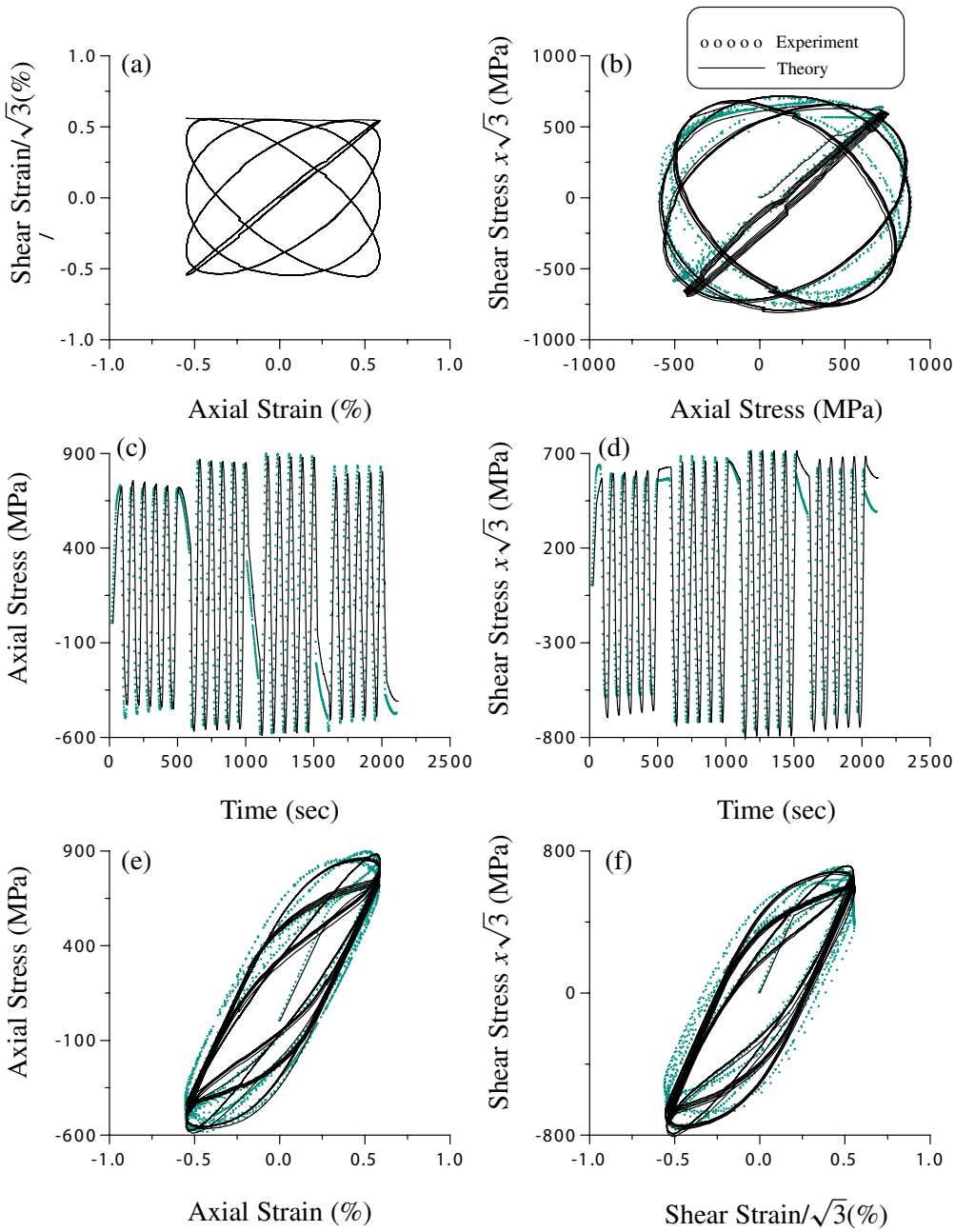

Figure 10. The experimental and simulated results of RHA under cyclic biaxial strain with input given in (a), and (b) the corresponding biaxial stress path, (c) time history of axial stress, (d) time history of shear stress, (e) axial stress versus axial strain, (f) shear stress versus shear strain.

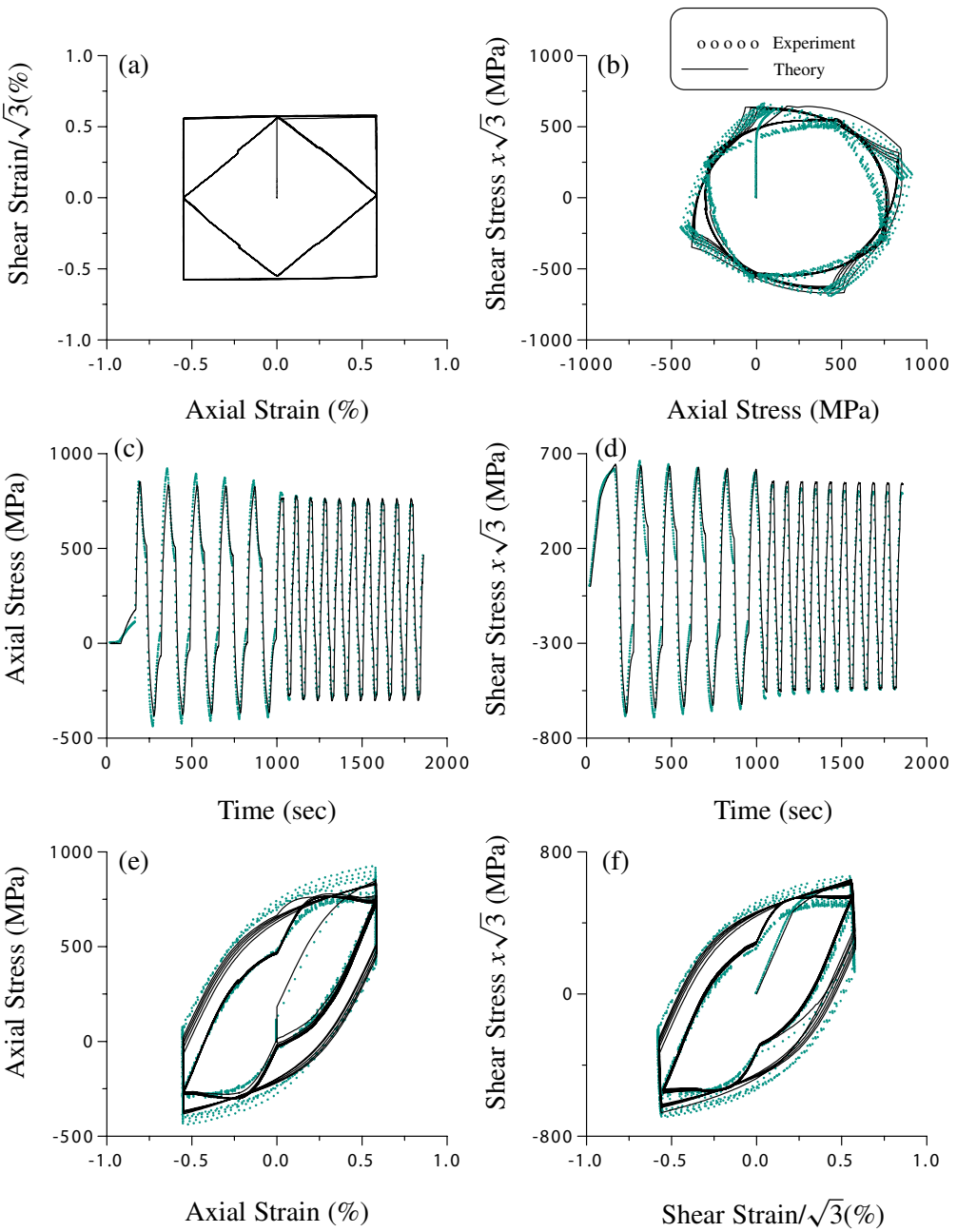

Figure 11. The experimental and simulated results of SAE 4340 under cyclic biaxial strain with input given in (a), and (b) the corresponding biaxial stress path, (c) time history of axial stress, (d) time history of shear stress, (e) axial stress versus axial strain, (f) shear stress versus shear strain.

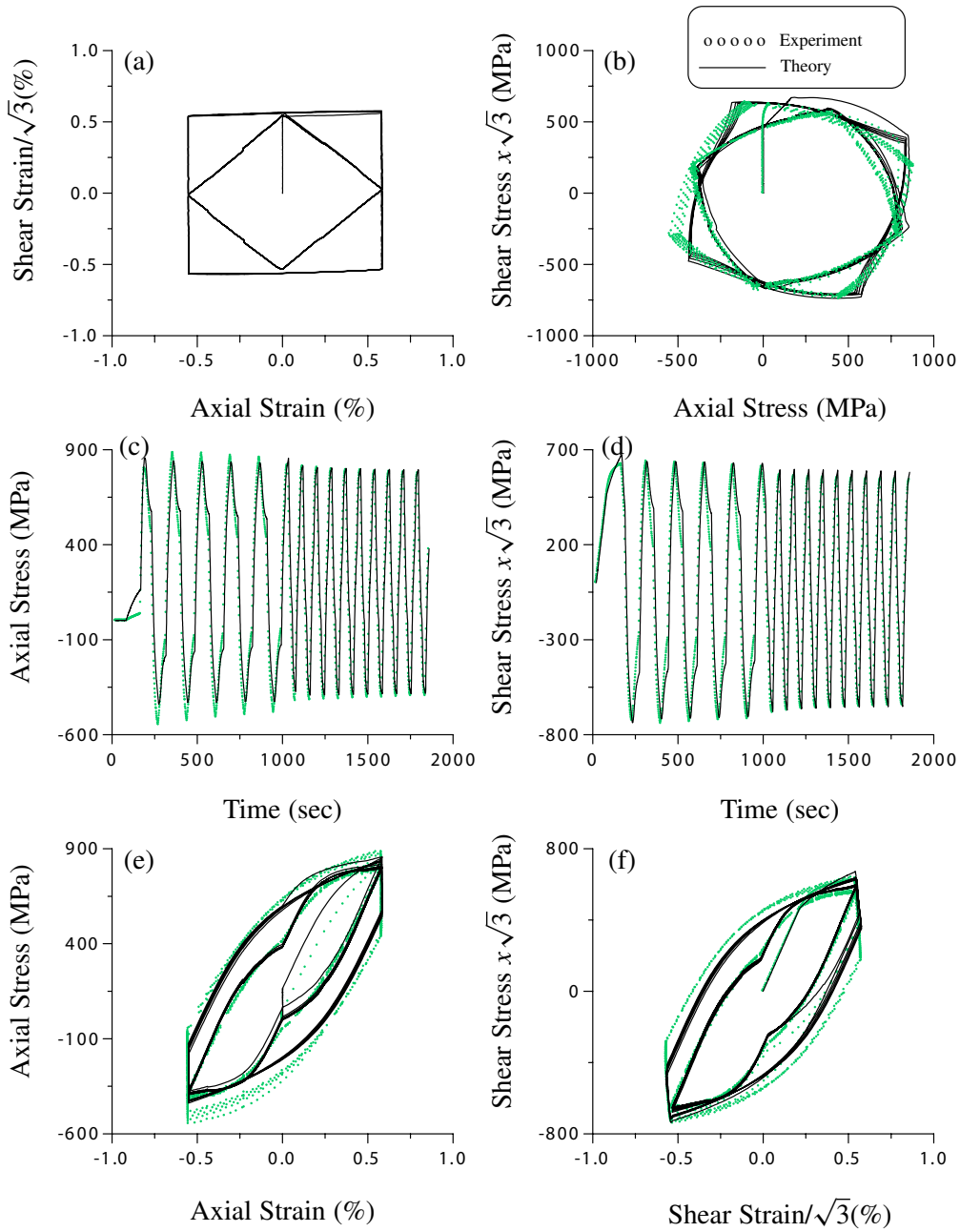

Figure 12. The experimental and simulated results of RHA under cyclic biaxial strain with input given in (a), and (b) the corresponding biaxial stress path, (c) time history of axial stress, (d) time history of shear stress, (e) axial stress versus axial strain, (f) shear stress versus shear strain.

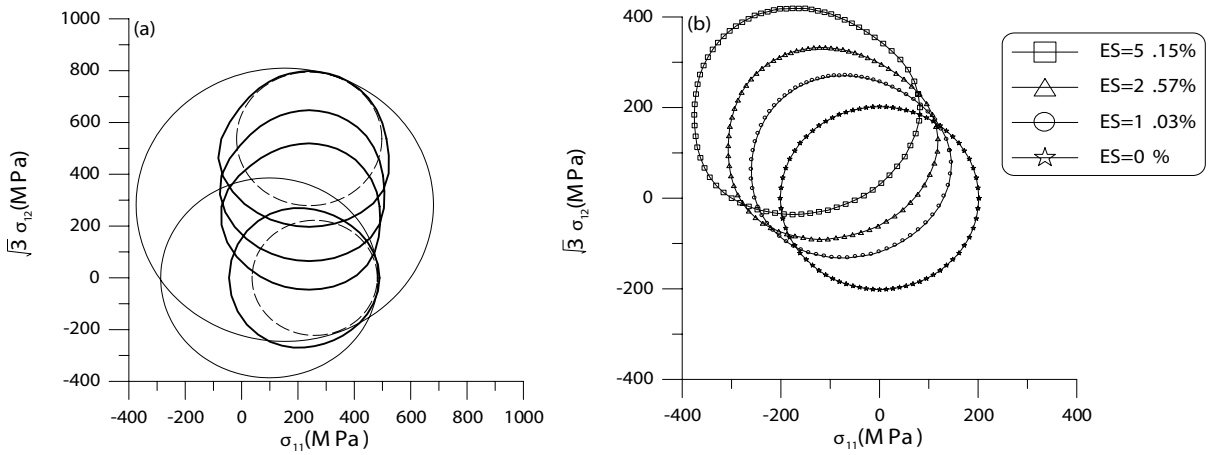

Figure 13. A theoretical prediction of yield surfaces with an equivalent strain offset with 0.001.

(2) For SAE 4340 and RHA, in the uniaxial cyclic tests subjected to a constant strain amplitude the cyclic stress-strain behavior tends to a steady state in the early stage of the test, and results in a stable hysteresis loop.

(3) For RHA in the uniaxial cyclic tests as shown in Figures 3 and 4, bottom, it behaves as an elastic-perfectly plastic material at the beginning of the yielding. According to the interpretation by Abdul-Latif [1996] for Waspaloy, a similar behavior of this sort is governed by a competition between softening (due to the isotropic softening) and the hardening (due to the kinematic hardening).

(4) The effect of mean strain for the constant strain amplitude tests seems less to affect the shape of the hysteresis loop.

(5) The cube type strain path may induce the stress relaxation in each direction. The relaxation in the axial direction is more significant.

(6) The effect of nonproportional strain paths is very pronounced in the biaxial cyclic tests of these two materials. Proportional loading results in a hysteresis loop which has the same shape as that for the uniaxial test. The highest stress response is obtained for a 90° out-of-phase loading. Complicated shapes of the hysteresis loops arise for both tensile and shear stresses in the nonproportional cyclic tests.

(7) In Figures 9c and 9d for the time histories of axial and shear stresses for SAE 4340, and in Figures 10c and 10d for the time histories of axial and shear stresses for RHA, an obvious softening cyclic phenomenon appears governed by the reduction in the loading path complexity, which changes from a 90° out-of-phase loading path to a 135° out-of-phase loading path. In a micromechanical view, this change leads to decreasing the number of activated slip systems in each plastified grain.

11. Numerical simulations

The conventional plasticity model may fail to simulate cyclic behavior properly, because the material functions used are only dependent on $\bar{e}^p$ alone. In cyclic loading conditions, $\bar{e}^p$ may be increased to a

large value. So the difficulty may arise when one wants to fit the material functions used in the cyclic response curves by using the data from a simple test.

In contrast, in the current two-complementary-trio model there exists a more flexible mechanism to control the increment of $\bar{e}^p$ through (71), of which the increasing of $\bar{e}^p$ can be reduced largely when the stress point is inside the bounding surface. In order to illustrate the proposed model response, the numerical simulations are presented below. The uniaxial cyclic strain paths and biaxial cyclic paths were designed to investigate the cyclic behaviors of SAE 4340 and RHA, including two tests in constant strain amplitude of 1.5% with the means of zero and 1.5%, a test with increasing amplitude and mean, the amplitudes of which start from 0.6% to 6% by adding 0.6% per cycle and with -0.6% fixed in the compression direction, and a cyclic test with increasing amplitude 0.5% per cycle but with mean zero.

The material functions used in this model have the following forms:

$$h_0(\bar{e}^p) = a_1 - a_2 e^{-a_3 \bar{e}^p} \text{ (MPa)},$$

$$h_a(\bar{e}^p) = a_4 - a_5 e^{-a_6 \bar{e}^p} \text{ (MPa)},$$

$$k_0' = a_7 - a_8 e^{-a_9 \bar{e}^p} \text{ (MPa)},$$

$$k_a' = (h_0' + k_0') \exp\left(a_{10}\left(\frac{\mathscr{D}}{2(h_0 - h_a)}\right)^{a_{11}}\right) - h_a' \text{ (MPa)},$$

$$G = a_{12} \text{ (MPa)}.$$

The other two material functions are given by $h_c = h_0 - h_a$ and $k_c' = k_a' - k_0'$. There are 12 material constants to be specified, one of which is the shear modulus of material. Table 2 lists the material constants for numerical simulations.

Figures 3–12, comparing numerical and experimental results, suggest that the overall behavior of these two materials SAE 4340 and RHA, as detected in this study, can be described very well. Phenomena covered by the description include the Bauschinger and Masing effects, cyclical hardening, saturation of stress, and out-of-phase hardening. Note that the material functions for each material used to simulate all four uniaxial tests and three biaxial tests are the same; no fine-tuning of the material functions was required in the simulations. Even for the long-term (20–30 cycles) prediction of this model, it still provides very good simulation results.

The comparisons of the biaxial cyclic test data and the numerical results calculated indeed provide very good prediction of the behavior of these two materials under nonproportional cyclic loading. Especially,

	G	a_1	a_2	a_3	a_4	a_5	a_6	a_7	a_8	a_9	a_{10}	a_{11}
unit	MPa	MPa	MPa	-	MPa	MPa	-	MPa	MPa	-	-	-
SAE 4340	72500	1453.8	3.2	34.8	100.2	-1.2	40	410	0.2	40	12.5	0.8
RHA	72500	1321	21	9.8	550	25	10	450	-50	10	8	0.8

Table 2. Material constants used in the numerical simulations.

the overhardening phenomena resulting from the nonradiality of the input strain path can be described very well by the proposed model.

12. Convexity of the distance function and yield surface with strain offset

For the linear path with $\dot{e}_{ij} = c_{ij}$ the switched-on time t_i for plasticity can be calculated by

$$t_i = \frac{\sqrt{2h_a^2/3}}{2G\sqrt{c_{mn}c_{mn}}}. \tag{72}$$

The integration of (3) with $\dot{e}^p_{ij} = 0$ from 0 to t_i gives

$$s_{ij}(t_i) = 2Ge_{ij}(t_i). \tag{73}$$

During this period of time, we have $s^b_{ij}(t_i) = s^b_{ij}(0)$ and

$$s^a_{ij}(t_i) = 2Ge_{ij}(t_i). \tag{74}$$

The substitution of the above equation and (72) into $s^a_{ij}(t_i)c_{ij}$ yields

$$s^a_{ij}(t_i)c_{ij} = \sqrt{2h_a^2 c_{mn}c_{mn}/3}. \tag{75}$$

From these equations the distance function is found to be

$$\mathscr{D} = -h_a - \frac{s^c_{ij}c_{ij}}{\sqrt{\frac{2}{3}c_{mn}c_{mn}}} + \sqrt{\frac{3(s^c_{ij}c_{ij})^2}{2c_{mn}c_{mn}} + h_a^2 + \frac{3}{2}s^c_{ij}s^c_{ij}}. \tag{76}$$

Assuming that the normalized condition $\frac{2}{3}c_{mn}c_{mn} = 1$ holds, we have

$$\mathscr{D} = -h_a - s^c_{ij}c_{ij} + \sqrt{(s^c_{ij}c_{ij})^2 + h_a^2 + \frac{3}{2}s^c_{ij}s^c_{ij}}. \tag{77}$$

Because of

$$\frac{\partial^2 \mathscr{D}}{\partial c_{ts}\partial c_{mn}} = \frac{h_a^2 + 3s^c_{ij}s^c_{ij}/2}{[(s^c_{kl}c_{kl})^2 + h_a^2 + 3s^c_{kl}s^c_{kl}/2]^{3/2}} s^c_{ts}s^c_{mn}, \tag{78}$$

the Hessian matrix of $\mathscr{D}$ is positive definite, and thus we have proved that the distance function $\mathscr{D}$ is strictly convex with respect to c_{ij}.

Consider a two dimensional strain path with $\dot{e}_{11} = \cos\theta$ and $\dot{e}_{12} = \sin\theta$. The distance function reads as

$$\mathscr{D} = -h_a - \|s^c_{ij}\|\cos(\theta - \beta) + \sqrt{[\|s^c_{ij}\|\cos(\theta - \beta)]^2 + h_0^2 - \|s^c_{ij}\|^2}, \tag{79}$$

where

$$\|s^c_{ij}\| := \sqrt{\frac{3}{2}s^c_{ij}s^c_{ij}}, \qquad \beta := \arccos\frac{s^b_{11} - s^d_{11}}{\|s^c_{ij}\|}.$$

It is easy to check that $\mathscr{D}$ as a function of θ is strictly convex.

For each linear path specified by $\dot{e}_{11} = \cos\theta$ and $\dot{e}_{12} = \sin\theta$, the increment of active stress and back stress before contact can be obtained, respectively, from (5) and (24):

$$\delta s^a_{ij} = 2G\delta e_{ij} - \Big(2G + \frac{2}{3}k'_a\Big)\frac{3\delta\bar{e}^p}{2h_a}s^a_{ij},$$
$$\delta s^b_{ij} = \frac{k'_a\delta\bar{e}^p}{h_a}s^a_{ij}.$$

Accordingly, we have

$$\|\delta s^a_{ij}\| = \frac{3Gh'_a\|\delta e_{ij}\|}{3G + h'_a + k'_a},$$
$$\|\delta s^b_{ij}\| = \frac{3Gk'_a\|\delta e_{ij}\|}{3G + h'_a + k'_a},$$

in which

$$\|\delta s^a_{ij}\| := \sqrt{\frac{3}{2}\delta s^a_{ij}\delta s^a_{ij}},\ \ \|\delta s^b_{ij}\| := \sqrt{\frac{3}{2}\delta s^b_{ij}\delta s^b_{ij}},\ \ \|\delta e_{ij}\| := \sqrt{\frac{2}{3}\delta e_{ij}\delta e_{ij}}.$$

The quantity $\|\delta e_{ij}\|$ is a prescribed offset of equivalent strain along the radial path, and $\|\delta s^a_{ij}\| + \|\delta s^b_{ij}\|$ is the corresponding stress increment induced by $\|\delta e_{ij}\|$. Consequently, the yield surface determined by the offset is given by

$$f(\theta) := h_a + \|\delta s^a_{ij}\| + \|\delta s^b_{ij}\| = h_a + \frac{3G\|\delta e_{ij}\|(h'_a + k'_a)}{3G + h'_a + k'_a},$$

From (70) and (79) the function $f(\theta)$ can be written as

$$f(\theta) = h_a + \frac{3G\|\delta e_{ij}\|(h'_0 + k'_0)\exp\Big(a(\frac{\mathscr{D}}{2h_c})^b\Big)}{3G + (h'_0 + k'_0)\exp\Big(a(\frac{\mathscr{D}}{2h_c})^b\Big)}. \tag{80}$$

For a prestrain of certain values of $\bar{e}^p$ and s^c_{ij} with a prescribed offset $\|\delta e_{ij}\|$, the above yield function can be determined.

Let us consider the following material functions:

$$h_0(\bar{e}^p) = 630 - 340e^{-7\bar{e}^p}\ \text{(MPa)},$$
$$h_a(\bar{e}^p) = 290 - 90e^{-6\bar{e}^p}\ \text{(MPa)},$$
$$k'_0 = 2500 - 500e^{-15\bar{e}^p}\ \text{(MPa)},$$
$$k'_a = (h'_0 + k'_0)\exp\Big(14\Big(\frac{\mathscr{D}}{2(h_0 - h_a)}\Big)^{1.5}\Big) - h'_a\ \text{(MPa)},$$
$$G = 27255.6\ \text{(MPa)}.$$

A theoretical prediction of the yield surfaces with a strain offset with 0.001 derived from Equations (80) and (79) is plotted in Figure 13a. We first apply a prestress to $\sigma_{11} = 481$ MPa, and then an elastic unloading to $\sigma_{11} = 228$ MPa. The first yield surface is plotted with thick black line, while the bounding

surface is plotted with a thin black line and the dashed line presents the surface of active stress s^a_{ij}. Consecutively, we plot the other three yield surfaces where the axial and shear stress are, respectively, $(\sigma_{11}, \sigma_{12}) = (306, 562)$ MPa, $(\sigma_{11}, \sigma_{12}) = (306, 687)$ MPa, and $(\sigma_{11}, \sigma_{12}) = (306, 837)$ MPa. The last bounding surface is also plotted with a thin black line and the dashed line is used to present the surface of active stress s^a_{ij}. It can be seen that the yield surfaces are gradually distorted from a circle to a convex curve with a front sharp and a rear flat. By the same token, in Figure 13b we plot the four yield surfaces along the 135° direction at the four different equivalent strains (ES) with $ES = 0\%, 1.03\%, 2.57\%, 5.15\%$. Similarly, the yield surfaces are gradually distorted from a circle to a convex curve with a front sharp and a rear flat.

The plastic deformation induced anisotropy was explicitly shown through the motion and distortion of the yield surface. The expansion in size, translation, distortion, and rotation of the yield surface strongly depend on the loading paths as shown in Figure 13, which reflect that the present model can simulate the strain-induced anisotropy of materials.

13. Concluding remarks

To effectively simulate the cyclic behavior of materials, a more tractable method to adjust the plastic modulus in the complex loading situation is needed. The combination of J_2 theory and the two-complementary-trio theory provides a good method to predict the material behaviors under cyclic loading conditions. For this model, we have demonstrated that the kinematic hardening rule is of the Prager type before contact or $\mathcal{D} = 0$. In the plasticity stage, before the contact of yield surface and bounding surface, the plastic flow is weak because $\mathcal{D} > 0$ in Equation (71), which renders the increment of $\bar{e}^p$ small. In order to avoid penetration, we have derived a contact rule about the motion of the contact surface. During the period of contact, the kinematic hardening rule is more complex and the plastic flow is large. The validity and accuracy of the new model were confirmed by comparing the numerical results with the experimental data for SAE 4340 and RHA materials under four uniaxial cyclic testings and three biaxial cyclic testings. Only 12 material constants were required in the new model, and it can be seen that the cyclic response curves described by the new model were in good agreement with the experimental data.

References

[Abdel-Karim 2005] M. Abdel-Karim, "Numerical integration method for kinematic hardening rules with partial activation of dynamic recovery term", *Int. J. Plast.* **21**:7 (2005), 1303–1321.

[Abdel-Karim and Ohno 2000] M. Abdel-Karim and N. Ohno, "Kinematic hardening model suitable for ratchetting with steady-state", *Int. J. Plast.* **16**:3-4 (2000), 225–240.

[Abdul-Latif 1996] A. Abdul-Latif, "Constitutive equations for cyclic plasticity of Waspaloy", *Int. J. Plast.* **12**:8 (1996), 967–985.

[Bari and Hassan 2001] S. Bari and T. Hassan, "Kinematic hardening rules in uncoupled modeling for multiaxial ratcheting simulation", *Int. J. Plast.* **17**:7 (2001), 885–905.

[Bari and Hassan 2002] S. Bari and T. Hassan, "An advancement in cyclic plasticity modeling for multiaxial ratcheting simulation", *Int. J. Plast.* **18**:7 (2002), 873–894.

[Bron and Besson 2004] F. Bron and J. Besson, "A yield function for anisotropic materials application to aluminum alloys", *Int. J. Plast.* **20**:4-5 (2004), 937–963.

[Cazacu and Barlat 2004] O. Cazacu and F. Barlat, "A criterion for description of anisotropy and yield differential effects in pressure-insensitive metals", *Int. J. Plast.* **20**:11 (2004), 2027–2045.

[Chaboche 1991] J. L. Chaboche, "On some modifications of kinematic hardening to improve the description of ratchetting effects", *Int. J. Plast.* **7**:7 (1991), 661–678.

[Chaboche 1994] J. L. Chaboche, "Modeling of ratchetting: evaluation of various approaches", *Eur. J. Mech. A Solids* **13** (1994), 501–518.

[Chen and Jiao 2004] X. Chen and R. Jiao, "Modified kinematic hardening rule for multiaxial ratcheting prediction", *Int. J. Plast.* **20**:4-5 (2004), 871–898.

[Chen et al. 2005] X. Chen, R. Jiao, and K. S. Kim, "On the Ohno–Wang kinematic hardening rules for multiaxial ratcheting modeling of medium carbon steel", *Int. J. Plast.* **21**:1 (2005), 161–184.

[Chiang et al. 2002] D.-Y. Chiang, K.-H. Su, and C.-H. Liao, "A study on subsequent yield surface based on the distributed-element model", *Int. J. Plast.* **18**:1 (2002), 51–70.

[Christensen 2006] R. M. Christensen, "Yield functions and plastic potentials for BCC metals and possibly other materials", *J. Mech. Mat. Struct.* **1**:1 (2006), 183–204.

[Dafalias 1984] Y. F. Dafalias, "Modelling cyclic plasticity: simplicity versus sophistication", pp. 153–178 in *Mechanics of engineering materials*, edited by C. S. Desai and R. H. Gallagher, John Wiley & Sons, New York, 1984.

[Dafalias and Popov 1975] Y. F. Dafalias and E. P. Popov, "A model of nonlinearly hardening materials for complex loading", *Acta Mech.* **21**:3 (1975), 173–192.

[Dafalias and Popov 1976] Y. F. Dafalias and E. P. Popov, "Plastic internal variables formalism of cyclic plasticity", *J. Appl. Mech. (Trans. ASME)* **98** (1976), 645–651.

[Dieng et al. 2005] L. Dieng, A. Abdul-Latif, M. Haboussi, and C. Cunat, "Cyclic plasticity modeling with the distribution of non-linear relaxations approach", *Int. J. Plast.* **21**:2 (2005), 353–379.

[Elgamal et al. 2003] A. Elgamal, Z. Yang, E. Parra, and A. Ragheb, "Modeling of cyclic mobility in saturated cohesionless soils", *Int. J. Plast.* **19**:6 (2003), 883–905.

[François 2001] M. François, "A plasticity model with yield surface distortion for non proportional loading", *Int. J. Plast.* **17**:5 (2001), 703–717.

[Hashiguchi 1988] K. Hashiguchi, "A mathematical modification of two surface model formulation in plasticity", *Int. J. Solids Struct.* **24**:10 (1988), 987–1001.

[Hashiguchi 1989] K. Hashiguchi, "Subloading surface model in unconventional plasticity", *Int. J. Solids Struct.* **25**:8 (1989), 917–945.

[Hassan and Kyriakides 1992a] T. Hassan and S. Kyriakides, "Ratcheting in cyclic plasticity, I: uniaxial behavior", *Int. J. Plast.* **8**:1 (1992), 91–146.

[Hassan and Kyriakides 1992b] T. Hassan and S. Kyriakides, "Ratcheting in cyclic plasticity, II: multiaxial behavior", *Int. J. Plast.* **8**:1 (1992), 91–146.

[Khoei and Jamali 2005] A. R. Khoei and N. Jamali, "On the implementation of a multi-surface kinematic hardening plasticity and its applications", *Int. J. Plast.* **21**:9 (2005), 1741–1770.

[Kowalczyk and Gambin 2004] K. Kowalczyk and W. Gambin, "Model of plastic anisotropy evolution with texture-dependent yield surface", *Int. J. Plast.* **20**:1 (2004), 19–54.

[Krieg 1975] R. D. Krieg, "A practical two surface plasticity theory", *J. Appl. Mech. (Trans. ASME)* **42** (1975), 641–646.

[Liu 2004] C.-S. Liu, "A consistent numerical scheme for the von Mises mixed-hardening constitutive equations", *Int. J. Plast.* **20**:4-5 (2004), 663–704.

[Liu 2005] C.-S. Liu, "Computational applications of the Poincaré group on the elastoplasticity with kinematic hardening", *Comput. Model. Eng. Sci.* **8**:3 (2005), 231–258.

[Liu 2006] C.-S. Liu, "Reconcile the perfectly elastoplastic model to simulate the cyclic behavior and ratcheting", *Int. J. Solids Struct.* **43**:2 (2006), 222–253.

[Liu and Chang 2004] C.-S. Liu and C.-W. Chang, "Lie group symmetry applied to the computation of convex plasticity constitutive equation", *Comput. Model. Eng. Sci.* **6**:3 (2004), 277–294.

[Liu and Chang 2005] C.-S. Liu and C.-W. Chang, "Non-canonical Minkowski and pesudo-Riemann frames of plasticity models with anisotropic quadratic yield criteria", *Int. J. Solids Struct.* **42**:9-10 (2005), 2851–2882.

[McDowell 1989] D. L. McDowell, "Evaluation of intersection conditions for two-surface plasticity theory", *Int. J. Plast.* **5**:1 (1989), 29–50.

[Mróz 1967] Z. Mróz, "On the description of anisotropic workhardening", *J. Mech. Phys. Solids* **15**:3 (1967), 163–175.

[Mróz et al. 1979] Z. Mróz, V. A. Norris, and O. C. Zienkiewicz, "Application of an anisotropic hardening model in the analysis of elasto-plastic deformation of soils", *Geotechnique* **29** (1979), 1–34.

[Mróz et al. 1981] Z. Mróz, V. A. Norris, and O. C. Zienkiewicz, "An anisotropic, critical state model for soils subjected to cyclic loading", *Geotechnique* **31** (1981), 451–469.

[Ohno and Abdel-Karim 2000] N. Ohno and M. Abdel-Karim, "Uniaxial ratchetting of 316FR steel at room temperature, II: constitutive modeling and simulation", *J. Eng. Mater. Technol. (Trans. ASME)* **122**:1 (2000), 35–41.

[Ohno and Wang 1991] N. Ohno and J.-D. Wang, "Transformation of a nonlinear kinematic hardening rule to a multisurface form under isothermal and nonisothermal conditions", *Int. J. Plast.* **7**:8 (1991), 879–891.

[Ohno and Wang 1993a] N. Ohno and J.-D. Wang, "Kinematic hardening rules with critical state of dynamic recovery, I: formulation and basic features for ratchetting behavior", *Int. J. Plast.* **9**:3 (1993), 375–403.

[Ohno and Wang 1993b] N. Ohno and J.-D. Wang, "Kinematic hardening rules with critical state of dynamic recovery, II: application to experiments of ratchetting behavior", *Int. J. Plast.* **9**:3 (1993), 375–403.

[Ohno and Wang 1994] N. Ohno and J.-D. Wang, "Kinematic hardening rules for simulation of ratchetting behavior", *Eur. J. Mech. A Solids* **13** (1994), 519–531.

[Phillips and Kasper 1973] A. Phillips and R. Kasper, "On the foundations of thermoplasticity — an experimental investigation", *J. Appl. Mech. (Trans. ASME)* **40** (1973), 891–896.

[Phillips and Moon 1977] A. Phillips and H. Moon, "An experimental investigation concerning yield surfaces and loading surfaces", *Acta Mech.* **27**:1-4 (1977), 91–102.

[Phillips and Sierakowski 1965] A. Phillips and R. L. Sierakowski, "On the concept of the yield surface", *Acta Mech.* **1**:1 (1965), 29–35.

[Phillips and Tang 1972] A. Phillips and J. L. Tang, "The effect of loading path on the yield surface at elevated temperatures", *Int. J. Solids Struct.* **8**:4 (1972), 463–474.

[Prager 1956] W. Prager, "A new method of analyzing stresses and strains in work-hardening plastic solids", *J. Appl. Mech. (Trans. ASME)* **23** (1956), 493–496.

[Rockafellar 1970] R. T. Rockafellar, *Convex analysis*, Princeton University, New Jersey, 1970.

[Tseng and Lee 1983] N. T. Tseng and G. C. Lee, "Simple plasticity model of two-surface type", *J. Eng. Mech. ASCE* **109** (1983), 795–810.

[Vincent et al. 2004] L. Vincent, S. Calloch, and D. Marquis, "A general cyclic plasticity model taking into account yield surface distortion for multiaxial ratchetting", *Int. J. Plast.* **20**:10 (2004), 1817–1850.

[Voyiadjis and Abu Al-Rub 2003] G. Z. Voyiadjis and R. K. Abu Al-Rub, "Thermodynamic based model for the evolution equation of the backstress in cyclic plasticity", *Int. J. Plast.* **19**:12 (2003), 2121–2147.

[Voyiadjis and Sivakumar 1991] G. Z. Voyiadjis and S. M. Sivakumar, "A robust kinematic hardening rule for cyclic plasticity with ratchetting effects, I. theoretical formulation", *Acta Mech.* **90**:1-4 (1991), 105–123.

[Voyiadjis and Sivakumar 1994] G. Z. Voyiadjis and S. M. Sivakumar, "A robust kinematic hardening rule for cyclic plasticity with ratchetting effects, II: application to nonproportional loading cases", *Acta Mech.* **107**:1-4 (1994), 117–136.

[Wu 2003] H. C. Wu, "Effect of loading-path on the evolution of yield surface for anisotropic metals subjected to large pre-strain", *Int. J. Plast.* **19**:10 (2003), 1773–1800.

[Wu 2005] H. C. Wu, *Continuum mechanics and plasticity*, Chapman & Hall/CRC, New York, 2005.

[Wu et al. 2005] P. D. Wu, S. R. MacEwen, D. J. Lloyd, M. Jain, P. Tugcu, and K. W. Neale, "On pre-straining and the evolution of material anisotropy in sheet metals", *Int. J. Plast.* **21**:4 (2005), 723–739.

[Yeh and Lin 2006] W.-C. Yeh and H.-Y. Lin, "An endochronic model of yield surface accounting for deformation induced anisotropy", *Int. J. Plast.* **22**:1 (2006), 16–38.

Received 26 Jun 2006. Accepted 9 Oct 2006.

CHEIN-SHAN LIU: csliu@mail.ntou.edu.tw
Department of Mechanical and Mechatronic Engineering, No.2, Beining Road, Taiwan Ocean University, Keelung 202-24, Taiwan

HONG-KI HONG: hkhong@ntu.edu.tw
Department of Civil Engineering, No.1, Sec. 4, Roosevelt Road, Taiwan University, Taipei 106-17, Taiwan

YA-PO SHIAO: ypshaio@mdu.edu.tw
Department of Computer Science and Information Engineering, Mingdao University, Changhua, Taiwan